Water Resources Research

RESEARCH ARTICLE
10.1029/2025WR039963

Microscale Heterogeneity in Fluid Distribution Patterns During Drainage of a Homogeneous Sand: Neutron Imaging Visualization and Model Limitations

Alexander Sternagel[1,2], Ashish Dinesh Rajyaguru[3], Luca Trevisan[4,5], Ralf Loritz[1], Pavel Trtik[3], Anders Kaestner[3], Brian Berkowitz[6], and Erwin Zehe[1]

[1]Karlsruhe Institute of Technology (KIT), Institute of Water and Environment, Hydrology, Karlsruhe, Germany, [2]Now at: Federal Institute of Hydrology, Koblenz, Germany, [3]PSI Center for Neutron and Muon Sciences, Villigen PSI, Switzerland, [4]Karlsruhe Institute of Technology (KIT), Institute of Water and Environment, Hydromechanics, Karlsruhe, Germany, [5]Now at: BoSS consult GmbH, Stuttgart, Germany, [6]Department of Earth and Planetary Sciences, Weizmann Institute of Science, Rehovot, Israel

Abstract We use neutron radiography to provide high-resolution images of water distribution patterns inside the pore space of a uniformly packed sand in a flow cell, during drainage, induced by a sequence of suction tensions. The experiments reveal the emergence of heterogeneous water distribution patterns within the pore space of the sand, although its corresponding retention function suggests homogeneity. This demonstrates that truly homogeneous water movement does not occur even under controlled laboratory conditions in an, as much as possible, homogeneous porous medium, and over dimensions of only a few millimeters. Furthermore, we conduct simulations with a Darcy-Richards model aimed at (a) capturing the overall 1D drainage process of the flow cell, to obtain a macroscopic perspective on the system using spatially averaged saturation levels, and (b) gaining a more detailed microscopic understanding of the internal 2D pore space processes and spatial distribution patterns during water drainage. Simulation results show that the model can reproduce the macroscopic 1D drainage process of the flow cell with high accuracy. However, the microscopic, heterogeneous 2D distribution of water observed inside the flow cell can be reproduced only qualitatively, after manually introducing local heterogeneities into the pore space. This highlights that the successful reproduction of macroscopic dynamics with a Darcy-Richards model does not imply that the model can accordingly capture truly heterogeneous process patterns on the microscale.

Plain Language Summary We examine how the spatial distribution of water is rearranged over time as water drains from sand. A thin, vertical flow cell, 20 mm × 20 mm, is filled with a uniformly packed sand, saturated with water, and then allowed to drain from below. Drainage is induced by increasing the degree of suction. A special imaging technique is used to obtain high-resolution images of the water distribution patterns over time. The experiments reveal the emergence of heterogeneous water distribution patterns within the pore space of the sand, although other measures of sand properties characterize it as homogeneous. These experiments demonstrate that uniform water movement does not occur even under idealized and well-controlled laboratory conditions. In parallel, we used a well-established theoretical model to numerically simulate the laboratory experiments. It is found that while the numerical simulations can reproduce the average, larger scale process of drainage, the simulations yield smaller-scale spatial distributions of water that can reproduce heterogeneous patterns only qualitatively, and by introducing additional empirical information. Our findings deepen understanding of the limitations of conventional numerical models for water drainage, which may be effective at a macroscopic level but fail to represent the internal dynamics of the system accurately.

Key Points:

- Neutron imaging reveals heterogeneous water distribution patterns in homogeneous porous media during drainage
- A system can be macroscopically well-described by a model under the assumption of homogeneity
- However, this does not imply that the system ultimately behaves in a truly homogeneous manner on the microscale

Correspondence to:
B. Berkowitz and E. Zehe,
Brian.Berkowitz@weizmann.ac.il;
erwin.zehe@kit.edu

Citation:
Sternagel, A., Rajyaguru, A. D., Trevisan, L., Loritz, R., Trtik, P., Kaestner, A., et al. (2025). Microscale heterogeneity in fluid distribution patterns during drainage of a homogeneous sand: Neutron imaging visualization and model limitations. *Water Resources Research*, *61*, e2025WR039963. https://doi.org/10.1029/2025WR039963

Received 13 JAN 2025
Accepted 3 SEP 2025

Author Contributions:
Conceptualization: Alexander Sternagel, Ralf Loritz, Brian Berkowitz, Erwin Zehe
Data curation: Ashish Dinesh Rajyaguru, Pavel Trtik
Formal analysis: Alexander Sternagel, Ralf Loritz, Anders Kaestner, Brian Berkowitz
Funding acquisition: Brian Berkowitz
Methodology: Alexander Sternagel, Ashish Dinesh Rajyaguru, Luca Trevisan, Ralf Loritz, Brian Berkowitz
Project administration: Alexander Sternagel, Ralf Loritz
Resources: Ashish Dinesh Rajyaguru, Luca Trevisan, Pavel Trtik, Anders Kaestner, Erwin Zehe
Software: Alexander Sternagel
Supervision: Brian Berkowitz, Erwin Zehe
Validation: Alexander Sternagel

1. Introduction

Pore-scale diffusion and advection processes play a crucial role in solute transport during water flow in the vadose zone. While determining leaching, retention, and mixing of different water and solute fractions, diffusion, dispersion and advection also influence macroscopic system behaviors, such as travel time distributions (Sprenger et al., 2019) and breakthrough curves (Sternagel et al., 2022). To visualize and analyze such local pore-scale processes in porous media, several experimental *in situ* and non-destructive imaging methods are available (Rabot et al., 2018). These include computer and X-ray tomography (CT) (Kaestner et al., 2008; Shokri & Sahimi, 2012), magnetic resonance imaging (MRI) (Koptyug, 2012; Ranzinger et al., 2020), or photographic

Visualization: Alexander Sternagel
Writing – original draft: Alexander Sternagel, Ashish Dinesh Rajyaguru, Luca Trevisan, Anders Kaestner, Brian Berkowitz
Writing – review & editing: Alexander Sternagel, Ashish Dinesh Rajyaguru, Luca Trevisan, Anders Kaestner, Brian Berkowitz

imaging of glass micromodels (Chen & Flury, 2005; Gouet-Kaplan & Berkowitz, 2011; Shokri, Lehmann, & Or, 2008). Photographic imaging of flow and transport processes inside a transparent glass micromodel is one of the simplest and most cost-effective methods; however, it provides only a relatively coarse resolution of centimeters to decimeters. CT methods, on the other hand, provide high-resolution images in the range of micrometers, but often require the addition of a contrast agent to clearly differentiate the fluid from the solid phase. Salt (e.g., CsCl, CaI_2) is a commonly used contrast agent, but it has the disadvantage of altering the density and viscosity of the fluid, and thus also the hydraulic conductivity of the medium, creating artifacts in the flow properties (Ranzinger et al., 2020). Magnetic resonance imaging methods can operate without contrast agents and work on spatial scales of tens of micrometers. However, a high iron content of porous media can negatively influence the accuracy of the MRI technology, and it generally works only in rather coarse porous media (Ranzinger et al., 2020).

Here, we explore neutron radiography as an alternative imaging method, from which we can derive detailed images of the pore space and its saturation state in the micrometer range. Neutron radiography can capture very small water amounts and fluctuations in porous media without the need for additional contrast agents, because the hydrogen atom interacts strongly with the neutrons at the atomic scale, creating a strong neutron attenuation at the continuum scale (Kaestner et al., 2008). Tumlinson et al. (2008) successfully applied the neutron imaging technology to soils, to describe the spatial distribution of pore water, roots, and root water uptake. Schaap et al. (2008) used neutron radiography to visualize the impact of structural connectivity on fluid flow in a sandy medium. They found that the method is particularly well-suited to demonstrate how interconnected and continuous structures influence the drainage behavior of a heterogeneous porous medium. Cheng et al. (2015) studied spontaneous water imbibition in unsaturated fractured Berea sandstone cores by neutron radiography, demonstrating that fractures can significantly increase imbibition effects by capillary action and surface spreading on fracture walls. These previous studies have shown that structural heterogeneities in porous media lead to heterogeneous water distribution patterns. In contrast, we aim here to investigate whether the drainage of a porous medium, structured as homogeneously as possible, will in turn ultimately lead, under controlled initial and boundary conditions, to uniform water distribution patterns or if microscale heterogeneity occurs nonetheless.

The question if homogeneity exists at all plays also a crucial role in soil-hydrological modeling where water flow dynamics in partially saturated soils are simulated using the common Darcy-Richards equation. This equation assumes that water flow is dominated by diffusive flow driven by capillary effects in the pore space (Bear, 1988). When applied to scales larger than the pore scale, Darcy-Richards models simplify the soil pore structure to a continuum. Under this simplification, specific heterogeneous effects in different pore sizes are not resolved, but they are averaged over the entire pore size distribution. This results in homogeneity of local hydraulic and retention characteristics for the simulation of water dynamics on this continuum scale (Berkowitz et al., 2016; Beven & Germann, 2013). Indeed, such a simplification of homogeneity has advantages for the applicability of Darcy-Richards models on larger scales where it has been proven useful to make valid predictions of actual water dynamics (Sternagel et al., 2019; Zehe et al., 2001; Zehe & Jackisch, 2016). However, modeling the overall flow dynamics on the continuum scale does not consider local pore scale properties like specific pore water chemistry, different water ages and resident times of distinct water pools, although they can have in turn potential implications on soils in natural environments (Li & Berkowitz, 2018). Thus, the homogeneity assumption of the Darcy-Richards theory can lead to an underestimation and smoothing-out of microscale influences and gradients across the pore space, resulting in biased predictions by these models (Sternagel et al., 2021, 2022).

Against this background, our study has two main objectives:

- In the first part (Section 3), we use neutron imaging (a) to unveil the hidden pore scale processes occurring during water drainage and distribution in an uniformly packed sand continuum, and (b) to evaluate the potential occurrence of heterogeneity effects on the microscale.
- In the second part (Section 4), we test the ability of Darcy-Richards models to describe the observed (a) macroscopic drainage behavior of the sand continuum, and (b) microscopic water distribution patterns inside the pore space of the sand. In particular, we examine situations in which these approaches fail and the consequences for the application of these models and the interpretation of their results. For simulations, we use the CATFLOW model (Maurer, 1997; Zehe et al., 2001) (Section 2.2).

Table 1
Flow Cell Geometry and S250 Sand Specifications

Flow cell geometry	
Height z (cm)	2.0
Length x (cm)	2.0
Width y (cm)	0.1
Volume (cm^3)	0.4
Mesh size of nylon filter (μm)	20
Mesh size of aluminum mesh (μm)	500
S250 specifications from experiment	
Height of sand in flow cell (cm)	1.60
Volume of dry sand in packed flow cell (cm^3)	0.32
Mass of dry sand in packed flow cell (g)	0.504
Density of dry sand in flow cell (g cm^{-3})	1.81
Water mass in saturated flow cell (g)	0.26
Water volume in saturated flow cell (cm^3) (at water density of 1 g cm^{-3})	0.26
Porosity calculated (−)	0.46
S250 specifications from manufacturer	
Type	Quartz sand (>99% SiO_2)
Non-compacted bulk density (g cm^{-3})	1.58
Particle density (g cm^{-3})	2.62
Porosity (−)	0.40
Particle size range (mm)	0.2 − < 0.04 (90% are ≥0.1 mm)

2. Methods

2.1. Experiments

2.1.1. Neutron Imaging Experiment

The aim of the neutron imaging experiment is to provide insights regarding water distribution patterns inside the pore space of a "homogeneous" sand pack during suction-induced drainage. To this end, we use a vertical, rectangular-shaped glass cell that is filled as uniformly as possible with a quartz sand (Table 1). Throughout the manuscript, we use the term "homogeneous" to indicate that we assume a macroscopically homogeneous, uniform sand packing in the flow cell, although we recognize that natural heterogeneity in fact exists across all scales. The sand in the cell is initially fully saturated with double deionized water (DDW, 18.2 MΩ cm^{-1}). Then, stepwise increasing suction tensions are applied at a bottom outlet using a vacuum pump. After each step, the system is allowed to re-equilibrate through drainage and internal water redistribution, before the suction tension is increased again.

Neutron imaging is used during this procedure to visualize the distribution of water inside the pore space of the sand as it drains gradually. Figure 1 shows the setup of the cuboid-shaped flow cell composed of quartz (glass), which was boron-free to avoid neutron absorption and related biases. Refer to Figure 1 and Table 1 for detailed geometrical data. The lower part of the flow cell is affixed to a slot positioned at the center of a cylindrical cell holder featuring threads. This cell holder is then threaded into a base plate, which includes a drainage channel that is connected to a vacuum pump. A nylon filter placed atop an aluminum mesh is positioned between the upper end of the drainage channel and the lower part of the cell holder. This arrangement serves to keep sand grains from exiting the flow cell during the experiment, but is sufficiently thin (<1 mm) and with a sufficiently large mesh size (∼100 μm) so as not to affect the hydraulic conductivity of the sand. The filled flow cell is then gently tapped to ensure a uniform distribution of the sand grains (see Section 3.1). Two of these flow cells are prepared, the first one being used for the actual neutron imaging experiment and the second one being employed for an additional

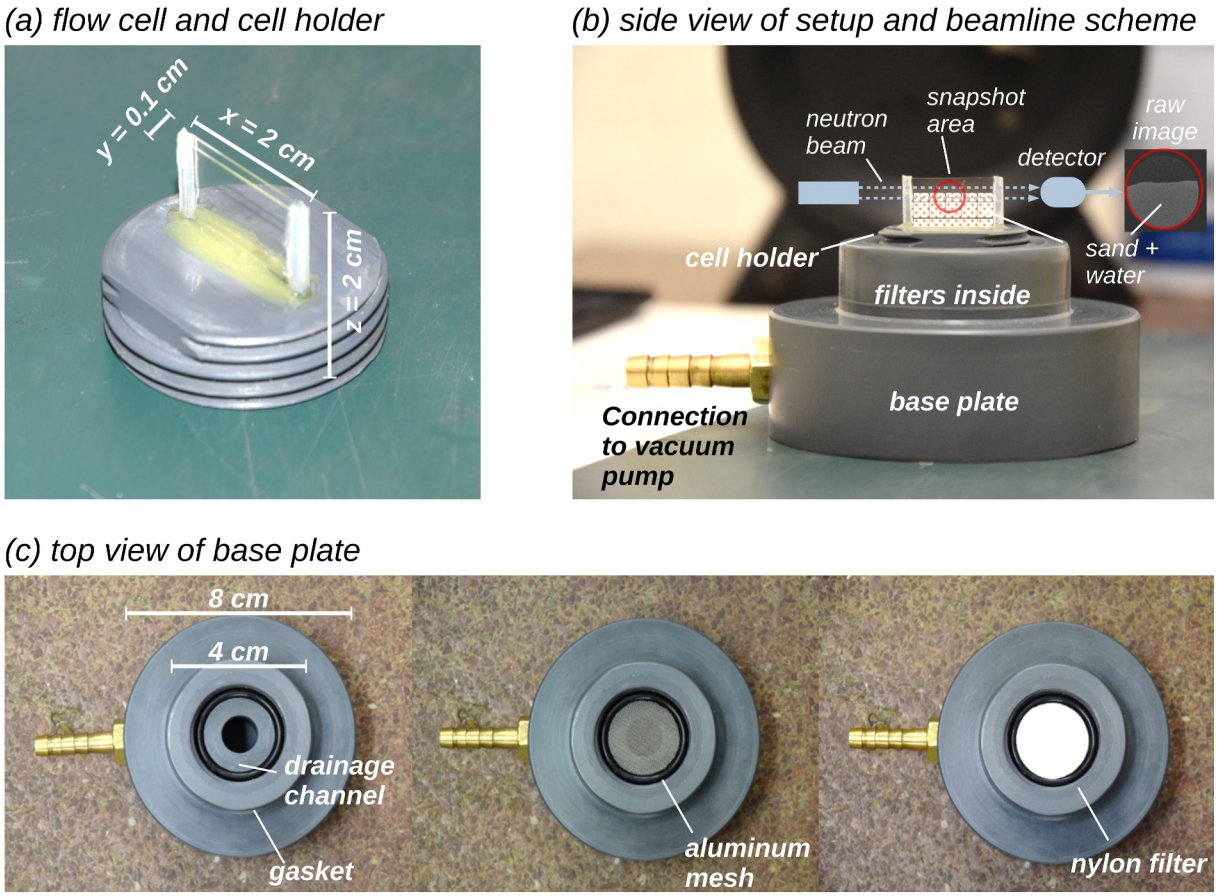

Figure 1. Setup of flow cell apparatus: (a) The flow cell is affixed to the cell holder with Araldite rapid glue. Only the top half of the flow cell (1 cm) remains visible, (b) side view of the setup including a schematic sketch of the beamline scheme, and (c) top view of base plate with drainage channel and the filters. Photographs taken by Luca Trevisan.

suction-driven drainage experiment. The bulk density is estimated by weighing the empty and packed flow cells, as well as bulk sand volume in the cells. The porosity is estimated by measuring the difference in weight of the packed flow cell without and with the addition of water, and then dividing by the volume of sand estimated from the bulk density.

For the neutron imaging experiment, a field of view (FOV) is set to observe, and record images, of a circular region at the interface of a pure air phase above the actual continuum (including the phases of sand, water and air) in the flow cell (see Section 3.1). Initially, DDW (denoted hereafter as "water") is applied carefully on the top of the flow cell until the pore space of the sand is fully saturated. The saturated flow cell is then subjected to a series of suction tensions to drain it via the bottom outlet, controlled by the vacuum pump. In a first phase, a tension of 0.016 MPa (low-suction) is applied for 248 min, followed by 1.14 MPa (mid-suction) for 227 min, and finally, 10 MPa (high-suction) for 397 min. Preliminary tests showed stable pressures throughout the duration of the measurements, over the range of suction values considered here.

Throughout the entire duration of the suction series, the designated FOV region is continuously exposed to a neutron flux with an intensity of 10^7 n cm^{-2} s^{-1} mA^{-1}, and the neutron source at SINQ (Blau et al., 2009) is operated at 1.35 mA. A back-end detector setup collects the neutron beams passing through the different materials (sand, water, air) of the flow cell and generates images of the internal pore structure with a pixel resolution of 5 μm at 1-min intervals (872 images in total). The back-end detector setup (Figure 2) consists of a camera-box (MIDI-setup) equipped with a CCD camera (Andor iKon-L) and a 100 mm objective (Makro-Planar 2/100ZF.2, Zeiss). A fiber optics taper (FOT) (Morgano et al., 2018) is attached to the camera-box to increase the spatial resolution of the imaging process. At the smaller end of the FOT, a scintillator screen (Gd2O2S:Tb;

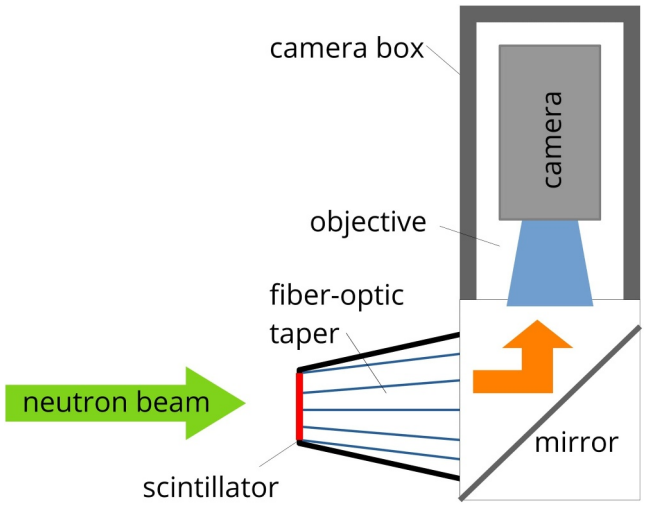

Figure 2. Schematic setup of the back-end detector, *after* neutron beams have passed through the sample.

RC-Tritec, Switzerland) with a thickness of 10 μm is mounted. The collimation L/D ratio equals to 365. The neutron imaging experiments are performed at the NEUTRA beamline facility (Lehmann et al., 2001), at measuring position number 2.

A neutron beam passing through the sample is attenuated according to the Beer-Lamberts law, which describes the relation between sample thickness and the composition of different phases. The quartz sand grains have a considerably lower attenuation coefficient than water. The quantification of water amounts in the porous medium requires the knowledge of the attenuation coefficient and an initial sample state, which is used as reference for a differential analysis of the changes in the water content. This approach provides the local thickness of water films and water volumes behind each pixel over time (Chapters 7 and 20 in Strobl & Lehmann, 2024). The upper boundary of the cell has an interface to the air and preliminary measurements have shown that water loss due to evaporation is negligible.

Appendix A contains additional information about the image analysis, with technical specifications for the pre-processing of the neutron experiments and the post-processing of the recorded image data.

2.1.2. Additional Suction-Driven Drainage Experiment

A second, identically prepared flow cell is employed for an additional suction-driven drainage experiment following the same experimental procedure as the previous one, except for the neutron imaging. The data obtained from this additional experiment allow the determination of the specific water retention and hydraulic conductivity characteristics of the S250 sand within the flow cell. This information is essential for calculating the simulation parameters for the subsequent modeling part.

The initially saturated flow cell again undergoes a series of suction tensions to drain it completely. However, this time, a finer resolution of suction tensions is applied, ranging from the previous low-suction (0.016 MPa) to mid-suction (1.14 MPa) values. Drainage occurs at specific suction tensions of 0 MPa, 0.016 MPa, 0.1 MPa, 0.3 MPa, 0.6 MPa, and 0.9 MPa, each for a duration of 1 hr. Following each suction step, the flow cell is weighed to quantify the amount of water that drained during that step. This experimental procedure is repeated multiple times to ensure the accuracy of the results.

2.2. Numerical Modeling

2.2.1. 1D Simulation of Flow Cell Drainage

As an initial step, we conduct 1D simulations aimed at capturing the overall drainage process of the entire flow cell during the experiments. These simulations are designed to offer a more macroscopic perspective on the average saturation levels throughout the entire flow cell as water progressively drains through the application of three suction tensions. However, they do not provide insights into the internal flow cell mechanisms. For this purpose, we use the CATFLOW model (Maurer, 1997; Zehe et al., 2001). For water dynamics in variably saturated porous media, the model numerically solves the Darcy-Richards equation in two dimensions (Equation 1).

$$\frac{\partial \theta}{\partial t} = \nabla[K(\theta) \cdot \nabla H], \tag{1}$$

with $\nabla H = \left(\frac{\partial(\Psi_m + \Psi_z)}{\partial x}, \frac{\partial(\Psi_m + \Psi_z)}{\partial z}\right)$. This represents the classical formulation for describing water flow between finite elements of a partially saturated flow domain, assuming lateral homogeneity. It focuses on changes in water content, $\partial\theta$ ($L^3\,L^{-3}$), within vertical, ∂z (L), and horizontal elements, ∂x (L), over a given time step, ∂t (T). Water fluxes result from spatial potential gradients ∇H, defined as the interaction between gravity potential, Ψ_z (L), and capillarity potential, Ψ_m (L). The hydraulic conductivity serves to scale these water fluxes and indicates how easily a fluid can traverse a porous medium (Bear, 1988).

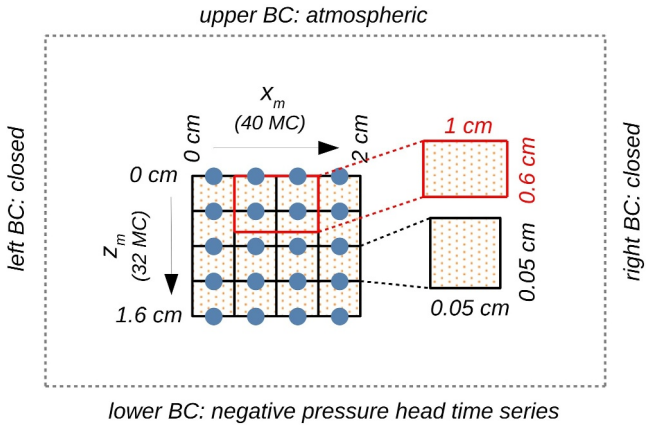

Figure 3. CATFLOW model setup. MC denotes the number of model cells the model exhibits in vertical z_m and horizontal x_m dimension. BC means boundary condition. The red rectangle highlights the field of view region (neglecting the air phase), which will be consulted for comparisons to observations (Section 3.2). Model simulations provide 2D images with a resolution of 20 MC per 1 cm and each MC has a dimension of 0.05×0.05 cm or 500×500 μm^2 (black rectangle).

The model is structured to align with the setup of the beamline experiments, utilizing the same flow domain geometry (see Section 2.2.2, Figure 3) and hydraulic properties of the S250 sand derived directly from the experimental findings. Importantly, no additional calibration is applied, and all relevant parameters can be found in Table 2. The 1D simulations involve modeling the vertical movement of water within an initially fully saturated flow domain (at θ_s), containing the "homogeneously packed" S250 sand, and breakthrough of water at the lower boundary. This is achieved by utilizing a uniform van Genuchten-Mualem (Mualem, 1976; van Genuchten, 1980). Single-porosity parameterization (Table 2). The upper boundary of the domain is open and set to atmospheric conditions (assuming a normal atmospheric pressure of 1013.25 hPa), with no infiltration, while at the lower boundary, a negative pressure head time series is directly applied in accordance with the suction tension sequence of the experiments. For 1D simulations, we focus only on the vertical dimension and quantify the water breakthrough at the lower boundary.

2.2.2. 2D Simulation of Internal Flow Cell Processes

Subsequently, we conduct 2D simulations of the drainage process, aiming for a more detailed microscopic understanding of the internal pore space processes during water drainage. The analysis here focuses on assessing whether the classical Darcy-Richards equation can reproduce the observed spatial water distributions patterns within the flow cell.

For these 2D simulations, we also employ the CATFLOW model. We apply a 2D simulation domain (1.6×2.0 cm) and discretize it into 32×40 model cells (MC), each with a size of 0.05×0.05 cm (Figure 3), allowing us to resolve water distribution both vertically and horizontally. The left and right boundaries of the domain are kept closed. Any further boundary conditions, parameterizations and model setups remain consistent with those used in the 1D simulations. We model the internal dynamics of the entire 2D flow cell, focusing on the FOV region for result analysis and comparison with observations, while excluding consideration of the air phase (highlighted by the red rectangle in Figure 3).

We explore the sensitivity of the internal water distribution and drainage behavior of the flow cell by applying different model assumptions and setups:

(i) Initially, we assume entirely homogeneous hydraulic conditions across the entire flow cell, parameterized using the hydraulic properties derived directly from the experiments, without further calibration.
(ii) Based on the previous results of (i) and observations, we make specific adjustments to the saturated hydraulic conductivity K_s values for certain regions within the flow cell. This adjustment is intended to mimic hydraulically inert regions in the pore space, which exhibit delayed drainage during the experiments (Section 3.2). Refer to the results section for the adapted K_s values.
(iii) We employ a random manipulation of hydraulic properties by applying a uniformly distributed random noise field for the K_s values across the entire flow cell, wherein the range of values is assigned to match the experimental results. In essence, each grid cell within the 2D flow domain is assigned a unique, random K_s value falling within the range of $\sim 3.24 \times 10^{-9} - 3.24 \times 10^{-5}$ m s^{-1}. With this assumption, we aim to test whether introducing stochastic elements into the model can produce similar patterns as achieved by the previous specific manipulation.

Table 2
Simulation Parameters

z_m (cm)	K_s (m s^{-1})	θ_s (m^3 m^{-3})	θ_r (m^3 m^{-3})	α (m^{-1})	n (–)	ρ_b (kg m^{-3})
1.6	3.24×10^{-5}	0.46 (experiment) 0.4 (manufacturer information)	0.0125	0.2012	2.296	1580

Note. z_m (m) is the vertical dimension of the flow cell, while the others are the van Genuchten-Mualem hydraulic parameters derived from the experiment results, where K_s is the saturated hydraulic conductivity, θ_s the saturated water content (=porosity, see Table 1), θ_r the residual water content, α the inverse of the air entry value, n a measure for the pore size distribution and ρ_b the bulk density of the S250 sand.

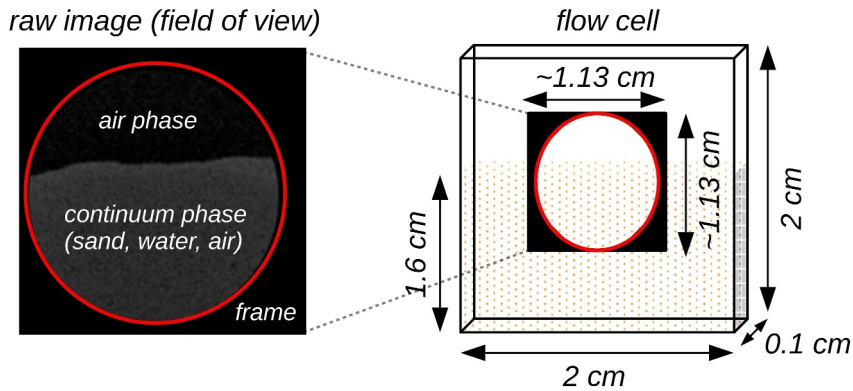

Figure 4. Schematic sketch of flow cell indicating the location of the field of view region at the interface between air phase and continuum phase (with sand, water and air) for neutron imaging. The brighter the color of a pixel, the wetter. Each image has an extent of 2048 pixels (5.54 × 5.54 μm) each in vertical and horizontal direction. Each pixel has an area of ∼30.7 μm^2.

For all simulation setups, we apply a gradual transition of suction tensions from low-suction (0.016 MPa) to mid-suction (1.14 MPa) over the duration of the mid-suction period (227 min). This assumes that the shift in suction tensions and the full unfolding of the tension effects on the pore space were not perfectly instantaneous processes but were delayed during the experiments. We use this assumption as a lumped representation of potential conditions that can limit the full effect of suction tensions on the flow cell; such conditions include restricted air infiltration due to clogging effects at interfaces, or internal hydraulic heterogeneities stemming from artificial compression during the sand packing process (Section 4.3).

2.2.2.1. Evaluation of Model Cell Size

For the simulation with the Darcy-Richards model, it must be ensured that a model cell is sufficiently large to assume a continuum. To evaluate this, we can calculate the volume and porosity of our model cell for a given sand grain number and size. By definition, a continuum can be assumed when the porosity is independent of the size and when the volume of the model cell is larger than the Representative Elementary Volume (REV) of the porous medium (Kutílek & Nielsen, 1994).

Our calculation scheme in terms of the REV is as follows: One model cell has dimensions of 0.5 × 0.5 × 1 mm, resulting in a volume of 0.25 mm^3. Assuming spherical-shaped sand grains with a diameter of 0.1 mm (according to the manufacturer, about 90% of the sand grains of the S250 sand are ≥0.1 mm), it yields a particle volume of 5.23×10^{-4} mm^3. Furthermore, the dimensions allow for a total of 250 grains (5 × 5 × 10 sand grains) with the assumed diameter (0.1 mm) to fit side by side into the model cell volume. The product of the number of grains and the volume of a single grain gives a total volume of 0.131 mm^3 sand grains in the model cell volume, or conversely, a pore volume of 0.119 mm^3 (0.25–0.131 mm^3), so that the porosity in a model cell is ∼0.47. Increasing the volume, while maintaining the grain size, results in the same porosity. Further, our model cell volume is larger than usual REV volumes of pure sand media. Costanza-Robinson et al. (2011), for example, found in their experiments with different sand-sized porous media REV volumes of down to 0.05 mm^3, equivalent to only 1 grain diameter. In contrast, the volume of our model cell is equivalent to 7.8 grain diameters, which is much larger. We thus deduce that the size of our model cell is sufficiently large to assume a continuum and justify application of the Darcy-Richards equation.

3. Results and Discussion of Experiments

3.1. Neutron Imaging Results

3.1.1. Raw Images

Figure 4 shows one example of the raw images of the observed FOV region that result from the neutron imaging experiments. Each of these images has an extent of 2048 pixels (∼1.13 cm) in both the vertical and horizontal direction, with each pixel measuring 5.54 × 5.54 μm^2. The image is divided into three phases: the air phase, the continuum phase (with sand, water and air), and a square frame that surrounds the actual circular image (in red).

We focus only on the continuum phase. In this phase, the pixels are brighter depending on the wetness of the sand at that location, indicating a higher resistance for the neutron beams during their passage.

Figure 5 presents raw images over time during the three suction phases, allowing us to observe the gradual drainage process of the pore space in the flow cell. At the beginning, a sharp boundary between the air phase and the continuum is evident, as the latter appears uniformly bright due to the initially fully saturated state of the flow cell. During the subsequent low-suction phase, no changes in the images can be observed, indicating that there is apparently no drainage of the flow cell. Additionally, there are no signs that water is evaporating from the upper interface of the continuum into the overlying air phase. The sharp boundary between the phases remains consistent throughout the duration of the initial phase and does not move downward. It is only with the start of the mid-suction phase at 249 min that changes become noticeable. Between 290 and 350 min, the pixels start to darken, indicating a gradual drainage of the pore space due to the mid-suction tension. This drainage process shows an inhomogeneous pattern across the pore space, with some areas draining more slowly than others. After 475 min at the end of the mid-suction phase, the image appears entirely black, suggesting that the pore space has been completely drained. Consequently, during the subsequent high-suction phase, no further changes can be observed. The mid-suction tension of 1.14 MPa was evidently sufficient to drain completely the pore space in the flow cell over a period of around 226 min.

3.1.2. Drainage Time Series

To quantify actual water amounts per pixel, a 2D matrix is generated for each raw image. The matrix has the same dimensions as the raw images, and each cell of the matrix contains a value indicating the water film thickness (in μm) in the corresponding pixel. By summing these water quantities in each pixel, the total water amount for each image can be obtained (Appendix A). This allows us to represent the overall drainage of the pore space in the images over time. Figure 6 depicts this drainage time series. For uniformity in treatment of measurements, data processing, as well as for comparison and interpretation between experiments, all values are presented in terms of normalized, relative water saturation values. Values are normalized by dividing the total water amount for each image (time) by the *initial* total water amount at the start of the experiment.

The original time series (in blue) exhibits fluctuations, possibly stemming from uncertainties in the neutron imaging procedure. A moving-average trend line is generated to smooth out these fluctuations. The progression of the drainage time series confirms the findings from Figure 5. The low-suction tension is evidently too weak to induce any drainage. The small apparent increase in water content in the low-suction phase might be due to measurement uncertainties or data post-processing (see Appendix B which further addresses drainage and water distribution fluctuations and heterogeneity). In contrast, the mid-suction tension results in a sudden onset of drainage immediately after its application, with a rapid and nearly complete drainage of the sand to a value of around 11% occurring over a period between 249 and 400 min. A difference from the previous results can be observed in the high-suction phase. The high-suction tension leads to a further drainage of residual, tightly bound water fractions, which are not visible in the black-and-white raw images in Figure 5. At the end (872 min), a residual water content of ∼3% is reached.

3.2. Post-Processed Analysis Results

In a post-processing step, the raw images in Figure 5 are further processed to ensure a better visualization of trends and patterns. We focus exclusively on the mid-suction phase because the previous observations indicated that this is the crucial phase of the drainage process. Using masking and clipping (Kaestner, 2022), the areas of the air phase and the frame are removed from the raw images, and the continuum is tinted in shades of blue. Additionally, a grid is applied to the images, which groups individual pixels to achieve a coarser resolution. Consequently, the following processed images are divided into 40×40 grid cells (GC), where 1 cm = 40 GCs, and each GC has a dimension of 50×50 pixels or $250 \times 250\ \mu m^2$. Each GC contains a relative water content (WC) value, normalized to the initial saturation state.

Figure 7 presents the processed images for the mid-suction phase. The "A-ratio" describes the fraction of clustered grid cells relative to the entire area of the continuum that are spatially connected (indicated by red rectangles) and have a WC value greater than the mean WC of the entire image at that time (as provided in the image headers). At the start of the mid-suction phase after 249 min, the continuum exhibits a homogeneous saturation state, serving as a reference. During the subsequent period between 290 and 350 min, three stable water pockets or

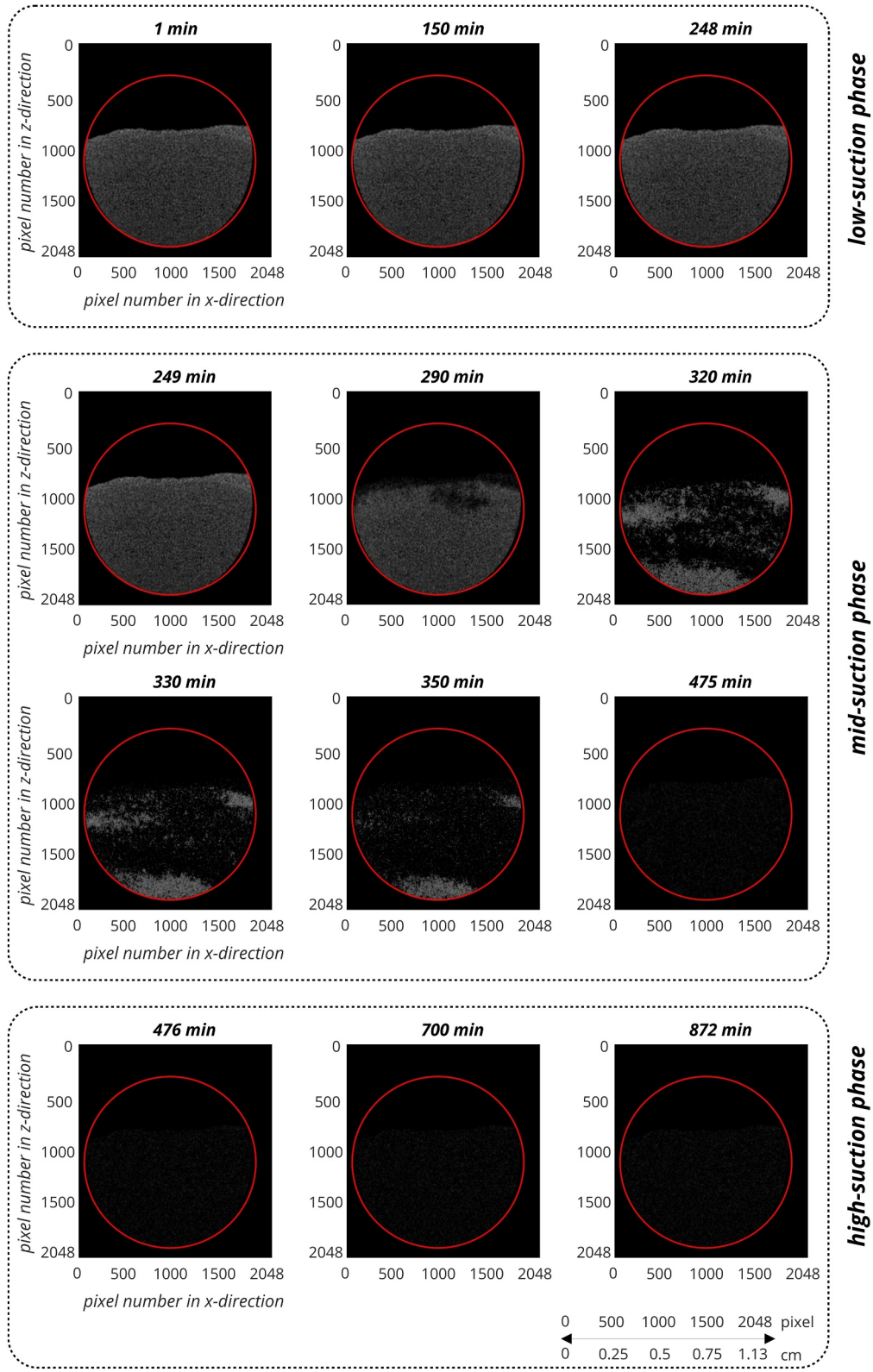

Figure 5. Observed raw images of the field of view region (red circle) over time showing the drainage process of the pore space in flow cell. Note the different intervals between images.

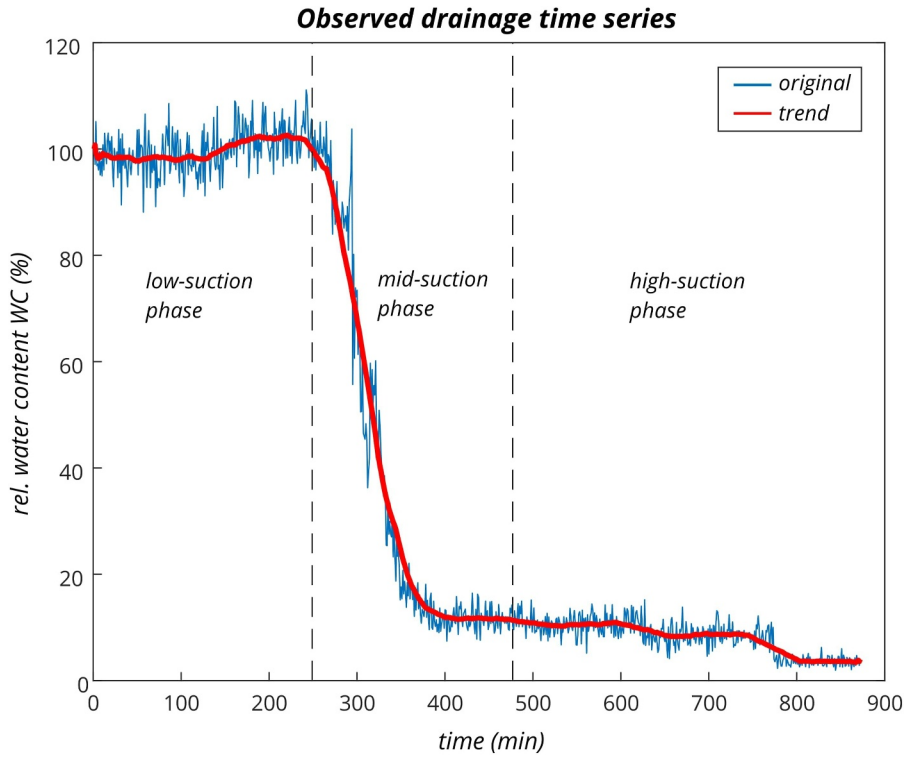

Figure 6. Observed drainage time series of the field of view region.

clusters (a–c) emerge as the drainage process takes place. These clusters drain significantly slower than the rest of the continuum, underlining the non-uniformity of the drainage process and corroborating the results of the observations (Figure 5). Water is retained in the three clusters and becomes temporally immobile. Consequently, the mean WC of the clusters is higher than the mean WC of the overall continuum. The bright areas between the clusters also indicate that they are largely separated from each other, and likely connected only by thin films along particle contacts. After 290 min, approximately 41% of the total area of the continuum is attributed to the three clusters. By 350 min, the three clusters still collectively occupy around 25.5% of the area, with many grid cells within these clusters having a WC value of nearly 100%, while the mean WC of the entire continuum drops to 30%.

Upon individual examination of the three clusters, differences in size and drainage speed become apparent. The initially largest cluster *a* (at 290 min) experiences the most significant decrease from an A-ratio of 18.2%–8.3% at 350 min. In contrast, clusters *b* (initially the smallest) and *c* (initially midsize) exhibit differences in size but both decrease by only ∼3% from 290 to 350 min, indicating a greater persistency compared to cluster *a*. Overall, cluster *c* is the largest as it is situated at the bottom of the image in the direction of the main downward drainage flux. At the end of the mid-suction phase (at 475 min), the clusters have vanished. The remaining water (11.0%) is once again uniformly distributed over the pore space. As an example, we calculate the Bond number for cluster *a* by choosing the characteristic length at the largest extent of the cluster, after 290 min (Figure 7), to evaluate if the system is dominated by capillarity or gravity in these stagnant regions (Hager, 2012). The value of ∼0.32, which is thus smaller than 1 and the maximum for all clusters, confirms that capillary forces dominate against gravity in the clusters representing the observed stagnation.

Appendix B contains additional post-processing analyses (Figures B1 and B2) of the observed images that further underline the heterogeneous nature of the drainage and water distribution process.

3.3. Derivation of Hydraulic and Retention Characteristics

The observed drainage behavior of the flow cell in the additional suction-driven water drainage experiment is depicted by the blue curve in Figure 8a. The corresponding suction tensions are converted from MPa to *m* (meters

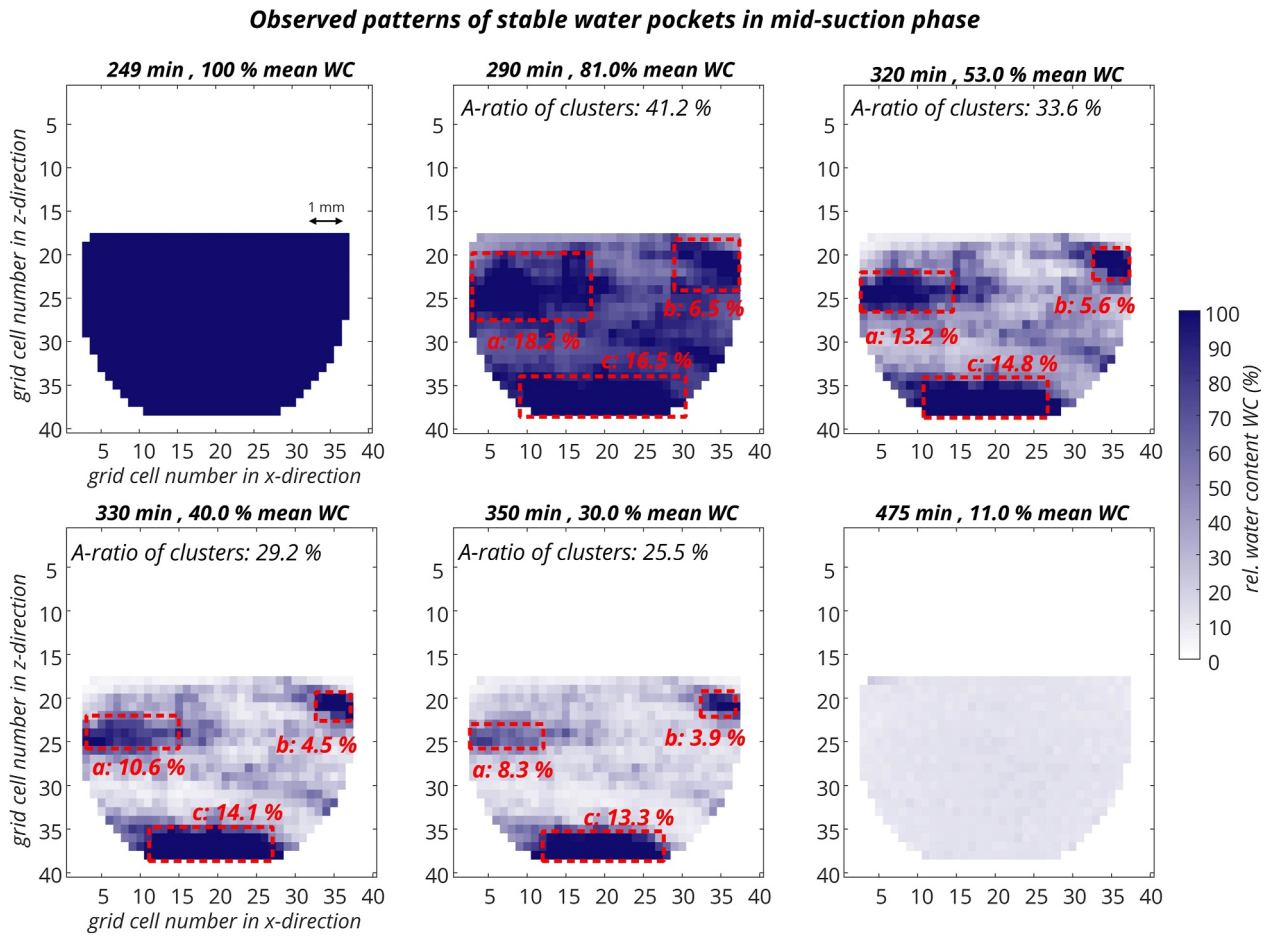

Figure 7. Patterns of stable water pockets in mid-suction phase. Three persistent clusters or stable pockets (a–c) are identifiable and their area share (A-ratio, in red) of the total continuum is presented. Summing these individual area shares gives a total A-ratio of all clusters at each time point. The length of 40 grid cells is equal to 1 cm.

of water column), which corresponds to the soil matric potential Ψ in the Darcy-Richards equation above (Equation 1). The relationship between relative water content WC (%) and matric potential Ψ (m) can be described in soil physics by an equation (Equation 2) after van Genuchten (1980) and Mualem (1976):

$$\mathrm{WC} = [1 + (\alpha\,\Psi)^n]^{-m}, \tag{2}$$

$$m = 1 - \frac{1}{n}$$

According to this equation, a corresponding relative water content value can be calculated for a given matric potential value, and vice versa, resulting in the characteristic retention curve shown in Figure 8a. The shape of this water retention curve is also determined by the shape parameters α and n. To determine these parameters, we employ a Monte-Carlo scheme and fit a theoretical curve (in red) to the observed curve. The best curve fit is achieved with the values $\alpha = 0.2012$ m^{-1} and $n = 2.296$. All relevant soil parameters are listed in Table 2.

Similar to the neutron experiments, the porosity (= saturated water content θ_s) of the S250 sand in the additional suction-driven water drainage experiment is determined to be 0.46, equivalent to a total water volume of 0.26 cm^3 in 0.54 g dry sand under fully saturated conditions. This value is somewhat larger than the value of 0.4 obtained from the manufacturer's official specifications, but within reasonable experimental variation. This aspect is discussed in Section 3.4. The residual water content θ_r remaining in the S250 sand after the application of the high-suction tension is approximately 0.0125, which is a realistic value for sand.

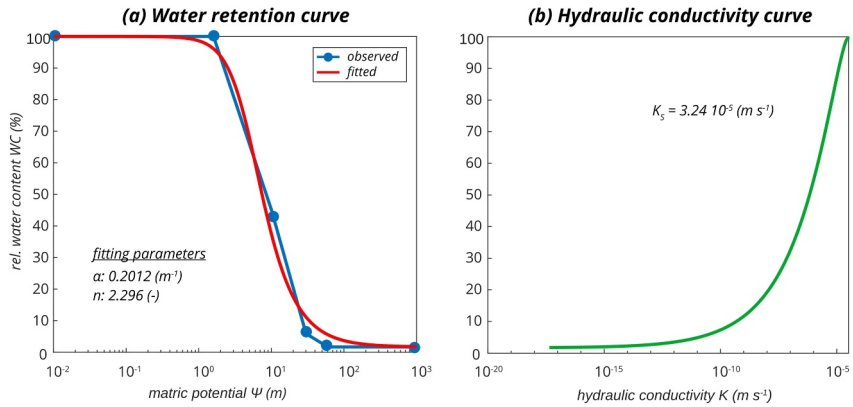

Figure 8. (a) Water retention curve (observed and fitted). The water masses remaining in the flow cell after each suction step are: 0 m–0.26 g, 1.6 m–0.257 g, 10 m–0.108 g, 30 m–0.015 g, 60 m–0.005 g, 90–0.001 g. Panel (b) shows the calculated hydraulic conductivity curve of S250 sand, derived from the additional suction-driven water drainage experiment (Section 2.1).

Furthermore, the additional suction-driven water drainage experiment yields a mean volume flux of 1.45×10^{-5} cm^3 s^{-1} (0.26 cm^3 of water drains over a duration of 5 hr). By relating that to the cross-sectional area of the flow cell (0.2 cm^2), this results in a mean velocity of the drainage of 7.25×10^{-5} cm s^{-1} or 7.25×10^{-7} m s^{-1}. We assume that this mean velocity corresponds to a rel. water content WC of 50%. With this assumption and Equation 3, we can calculate a theoretical hydraulic conductivity curve for the S250 sand, shown in Figure 8b:

$$K(\mathrm{WC}) = K_S\, \mathrm{WC}^{0.5} \left[1 - \left(1 - S^{m^{-1}}\right)^m\right]^2 \tag{3}$$

From the hydraulic conductivity curve, we can derive a saturated hydraulic conductivity K_S value of 3.24×10^{-5} m s^{-1}, which falls within a reasonable range for sand. These retention and hydraulic soil parameters (Table 2) will be needed for the subsequent simulation part.

3.4. Insights From the Neutron Imaging Experiments

The observed overall drainage time series (Figure 6) initially suggests a homogeneous drainage behavior of the flow cell, as expected according to the flow cell setup. With the onset of the mid-suction tension, the flow cell continuously drains until reaching the residual water content. However, this homogeneous behavior applies only under the macroscopic view of the general drainage time series of the flow cell. Under a microscopic view of the system, resolving the internal 2D structure of the pore space during drainage by the neutron imaging, a completely different picture emerges. The analysis results (Figure 7) reveal a non-homogeneous, discontinuous drainage behavior in the supposedly "homogeneous" sand and the establishment of heterogeneous patterns with stable water pockets. These water pockets are segregated from each other over the small scale of a few millimeters, without a significant connection through a water film bridge between them. This means that there is no or only reduced diffusive water exchange between water pockets. Within the stable water pockets, there are even isolated pore regions that remain fully saturated up to 350 min after the start of the experiment, while the surrounding bulk sand is almost completely dried out. The increasing influence of the air phase and its interplay with the liquid phase during the desaturation process leads to increased heterogeneity. This process likely causes the water to percolate mainly through the pore regions between the stable water pockets, which is a form of preferential flow. This heterogeneous distribution of fluid storage and flow under partially-saturated conditions can further lead to strongly anomalous transport behaviors (Cortis & Berkowitz, 2004; Velásquez-Parra et al., 2022).

Our findings are in line with the work of Gouet-Kaplan and Berkowitz (2011), who conducted flow experiments in a glass micromodel to explore old-new water exchange dynamics. They found stable pockets of tracer even at longer time scales and after multiple cycles of infiltration. Similar results were also found in

several field experiments, which were conducted to analyze the age of water compartments in hydrological systems on the plot (Turton et al., 1995) to catchment scale (Collins et al., 2000; Kirchner et al., 2000; Sklash et al., 1986). They all found significant amounts of old, persistent water remaining in the system that is only slowly leaving over a long time after an initial rapid flush. The experiment results of Hoffman et al. (1996), Oswald et al. (1997), and Menon et al. (2007) furthermore show the occurrence of heterogeneity in terms of fluid distribution and flow paths in homogeneous porous media on the scale of a laboratory column. On the same scale, Hoogland et al. (2015) revealed through neutron radiography that during rapid drainage rates, water is retained in certain high-saturation zones behind the drainage front due to viscous limitations. Shokri, Lehmann, Vontobel, and Or (2008), using neutron technology, found that even during slower evaporative drying, heterogeneities occur in the distribution of water above the drying front, with isolated clusters of high water content. The neutron imaging experiments presented here align with these previous studies and complementarily demonstrate heterogeneity of water storage and movement also on very small scales of micrometers to a few millimeters.

The derivation of the retention and hydraulic properties of the S250 sand for the subsequent simulations based on the experiment results yields relatively realistic parameter values (Table 2, Figure 8), except for the value of α. With regard to the porosity,the manufacturer of the S250 sand indicates porosity of 0.4, reasonably close to the value of 0.46 determined by replicate measurements in the flow cell. We note that the porosity value variations are likely a result of our specific flow cell setup with its very small dimensions: packing sand in a relatively small cell requires care, and the sand cannot be compressed too hard to avoid damaging the cell. The resulting porosity can thus be expected to be somewhat larger than that for a sand pack in a larger domain. Note, too, that we are of course cognizant of measurement uncertainty, and we thus interpret the experiments in terms of relative saturation, using the estimated porosity to examine absolute water contents.

Furthermore, the best fit of the water retention curve (Figure 8a) yields a value for α of 0.2012 m^{-1}, which is clearly lower than typical α values for sandy soils, indicating a relatively small pore size maximum. Carsel and Parrish (1988) estimate a value for α of 14.5 m^{-1} for an almost pure sandy soil. Possible reasons for these deviations could be boundary effects at the interfaces between sand and the glass walls, or the filling of the flow cell with water may have led to a small water surplus layer on the sand surface. Both situations would result in more water being present in the flow cell than it can be actually stored in the pore space of the sand. In general, the smaller the flow domain, the more dominant boundary effects become (Ranzinger et al., 2020). However, this difference has no significant influence on the following simulation results, as the very small extent of the flow cell and the relatively strong mid-suction tension lead to very rapid drainage in any case, regardless of whether a little more or less water is in the pore space. The very small α value can also be interpreted as an indication of clogging effects in the pore space, and associated limited air infiltration, especially in the regions of the stable water pockets. Such clogging effects are known to lead to a decreased permeability in porous media (e.g., Elrahmani et al., 2023; Tang et al., 2020), and therewith dampening the influence of suction tensions on the drainage process of the pore space in our experiments. This supports our assumption of a gradual, delayed transition of the suction tensions for the subsequent simulations, as further discussed in Section 4.3. We can further only speculate that the formation of the stable water pockets and the clogging effects in the porous medium might be attributed to mechanical disturbances in the pore structure, due to strains that lead to compaction of the pore space when increasing the suction tensions. Unfortunately, we are unable to derive further detailed information about the pore structure in the regions where the stable water pockets emerge from pre-experimental dry scans (Appendix A), due to the scan resolution and the low attenuation of glass and sand. This technical issue should be considered in future developments of flow cells for such neutron experiments.

4. Results and Discussion of Simulations

4.1. Simulation of 1D Drainage Time Series

Figure 9 presents the simulation results of the 1D drainage time series of the flow cell, in comparison to the observed time series. It should be noted that the observed time series reflects the drainage of the FOV region, while the model simulates the overall drainage of the entire flow cell. We compare both results by assuming that the timing and shape of the drainage time series of the entire flow cell are similar to what is observed in the FOV region. This assumption is reasonable due to the small dimensions of the flow cell, the uniform application of

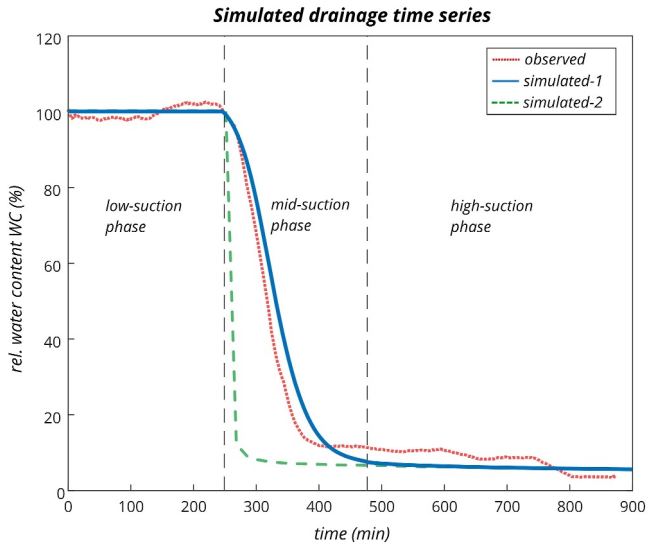

Figure 9. Drainage time series simulated with CATFLOW applying a gradual transition of suction tenions (*simulated-1*) and an instantaneous switch of suction tensions (*simulated-2*).

suction tensions over the cross-section of the bottom of the flow cell, and the "homogeneous" sand packing. The model utilizes the retention and hydraulic parameters derived directly from the experiments without further calibration (Table 2). The results show that the CATFLOW simulation applying a gradual transition of suction tensions (*simulated-1*) achieves a good match with the drainage time series observed in the experiments. It closely resembles the shape of the soil water retention curve (Figure 8a). In addition, we conduct a simulation with the assumption of an instantaneous switch of the suction tensions from low-to mid-suction (*simulated-2*). This setup results in a faster and almost instantaneous desaturation of the flow cell after switching to the mid-suction tension. For all simulations, the use of a homogeneous or heterogeneous distribution of internal retention and hydraulic parameters, according to assumptions (i–iii), does not significantly affect the overall simulated drainage time series. The effect of the suction tensions is predominant for the overall drainage process of the flow cell.

4.2. Simulation of Internal 2D Water Distribution During Drainage

Figure 10 presents the results of the CATFLOW 2D simulations of water distribution patterns inside the flow cell in mid-suction phase. Appendix C additionally contains CATFLOW 2D simulation results of internal water distribution patterns over time in the mid-suction phase, which support these findings.

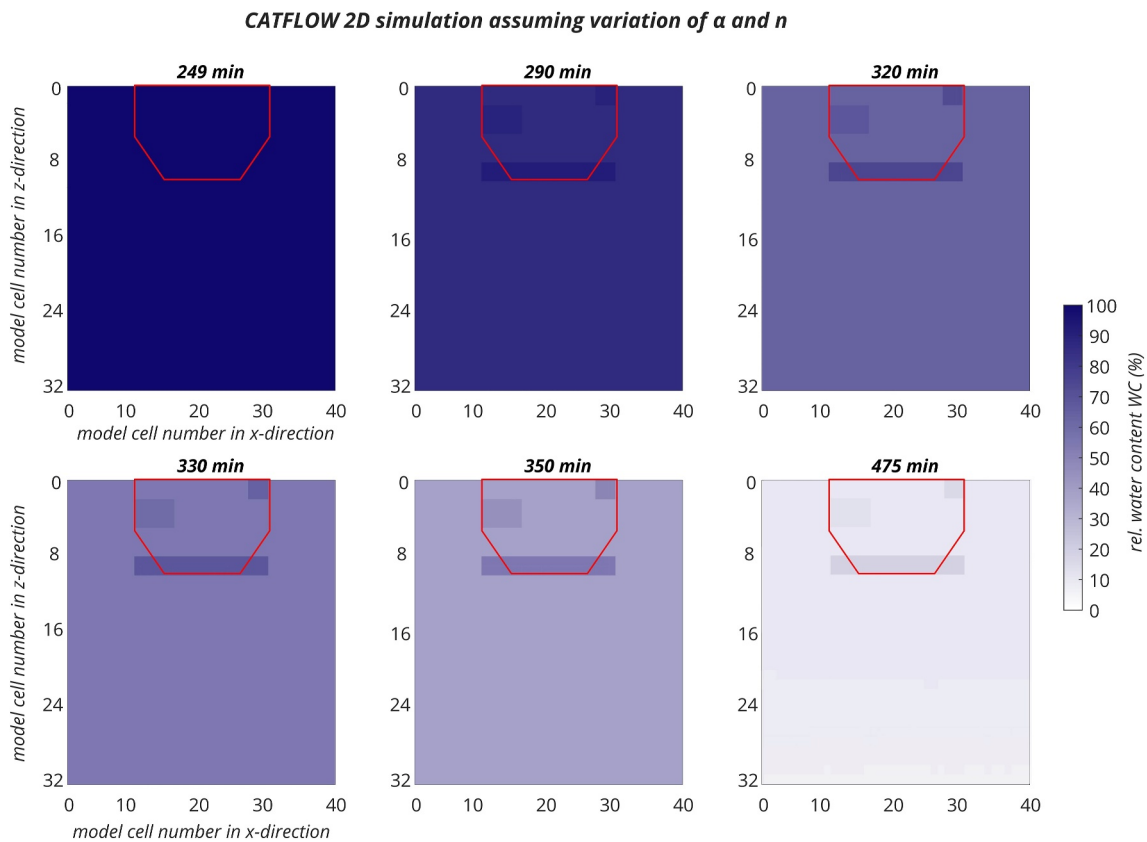

Figure 10. CATFLOW 2D simulation results of internal flow cell processes over time in mid-suction phase, based on an additional simulation setup with the application of specifically adapted values for α and n in the pore regions of the stable water pockets.

Figure 10 presents 2D water distribution patterns over time in mid-suction phase simulated with specifically adapted values for α and n in the pore regions of the stable water pockets. The values for α range from 0.1652 to 0.1852, and for the n parameter, the values range from 1.996 to 2.196 in the three stable water pockets. The remaining soil parameters for the bulk region of the continuum remain unchanged according to the values in Table 2. This also includes the K_s value, which remains constant at 3.24×10^{-5} m s^{-1} throughout the continuum, including the stable water pockets. With this setup, similar heterogeneous patterns in the continuum can be simulated by slight variations of the two parameters α and n (see also discussion in Section 4.3). The simulated images have a resolution where 1 cm = 20 model cells (MC), with each MC having a dimension of 500×500 µm. Each simulation image represents the entire extent of the flow cell. The red frame outlines the FOV region inside the continuum.

4.3. Insights From Simulations

The simulations with the Darcy-Richards model (CATFLOW), employing the parameters derived from the neutron experiments without additional calibration, match the observed drainage time series of the flow cell reasonably well, assuming a gradual transition between suction tensions (*simulated-1* in Figure 9). The additional simulation, in comparison, applying an instantaneous switch of suction tensions (*simulated-2* in Figure 9), overestimates the effect of suction tensions on the desaturation behavior of the flow cell. However, as we can see from the observed experimental results (drainage time series in Figure 6), instantaneous desaturation of the flow cell after switching to the mid-suction tension does not occur in reality. We suggest that the reasons for this are enhanced boundary effects in the very small flow cell and compaction of the pore space due to strains during the suction process. These may cause clogging effects, preventing the full suction tension effect from spreading instantaneously across the entire continuum. We account for this in our simulations by assuming a gradual transition of the suction tensions.

In contrast to the simulation of the drainage time series, CATFLOW cannot replicate the observed internal water distribution patterns during drainage (see assumption (i) and Appendix C, Figure C1). However, this is not surprising, as the flow domain is initially completely homogeneous. Subsequently, we manually add local heterogeneities to assess the model's ability to reproduce the observed patterns at least qualitatively. While this is possible (see assumptions (ii and iii) and Appendix C, Figures C2 and C3), stable pockets emerge only when using saturated hydraulic conductivity values four magnitudes smaller ($\sim 10^{-9}$ m s^{-1}) than the experimentally derived mean value (3.24×10^{-5} m s^{-1}). This appears to be unreasonable for a pure sand medium, but it is consistent with the very small α value (Section 3.4). Note that we obtain similar heterogeneous patterns by locally adjusting the soil parameters α and n, as shown in Figure 10; by adjusting the spatial distribution of α and n in the simulations, potential effects of capillary barriers in specific pore space regions can be represented.

Our simulations reveal that the Darcy-Richards model is indeed capable of representing well the macroscopically observed 1D drainage behavior of the system, even without calibration and assuming homogeneity. However, the observed 2D microscale variations can be reproduced, at best, only qualitatively. We note that a more precise simulation of the microscale patterns might be possible, though challenging, by using a more complex Darcy-Richards model that resolves structural heterogeneities not only spatially but also temporally. This leaves us with the crucial insight into the general limitation of common Darcy-Richards models and the continuum approach. Even though a system can be macroscopically well-described by a Darcy-Richards model under the assumption of homogeneity, this does not imply that the system ultimately behaves in a truly homogeneous manner on the microscale.

The findings presented here are in line with the results of other simulation studies (Berkowitz & Hansen, 2001; Edery et al., 2014; Li & Berkowitz, 2018; Schaap et al., 2008). Schaap et al. (2008) used a 2D Richards model to simulate the effect of structural connectivity on flow patterns in a sand medium, which they initially visualized through neutron imaging experiments, too. They concluded that the model is not capable of reproducing the observed flow patterns due to the assumption of a homogeneous air entry behavior, represented by a uniform α parameter. The simulations of Li and Berkowitz (2018) also demonstrate that stable water pockets exist on the pore scale and delineate a connection to larger field scales. The coexistence of different water pockets, composed of new, infiltrating water and old, resident water, in the soil significantly influences the availability and chemical signature of water for plant uptake, runoff, and groundwater recharge. Our results show that the observed microscale heterogeneities in the continuum do not invalidate the

applicability of the Darcy-Richards equation for successfully simulating the macroscale desaturation behavior. However, we suggest that this is not the case when focusing on solute transport. In an earlier study (Sternagel et al., 2022), we demonstrated that microscale diffusive mixing of substances across the pore space significantly affects the solute breakthrough curve (BTC) of an entire soil column, as water resides for different durations in different pore sizes, also impacting solute concentrations. Here, in our case, dissolved substances would accumulate and mix with water in the stable pockets, being flushed out only with a delay, resulting in a BTC with a non-Fickian shape, characterized by a longer tailing after the peak than what we observe here for pure water. This assumption is supported by the study of Edery et al. (2014), who showed the occurrence of preferential flow paths in a fully saturated porous medium, with large areas of the domain not engaged, resulting in a non-Fickian breakthrough curve that can ultimately converge, over extremely long times/distances, to a "normal" Fickian shape. At the same time, the internal spatial distribution of tracer within the porous system remains non-homogeneous, just as in our continuum.

5. Conclusions and Outlook

Neutron imaging experiments on the pore scale of a pure sand medium reveal that water does not redistribute homogeneously during the drainage of the flow cell, over dimensions of a few millimeters. Despite using "homogeneous" sand under controlled initial and boundary conditions, heterogeneous patterns of stable water pockets are observed inside the pore space of the sand, where water becomes temporarily immobilized. These experiments demonstrate that truly homogeneous water movement does not occur, not even under controlled laboratory conditions in a "homogeneous" porous medium.

Subsequent simulations of the experiments with a common Darcy-Richards model show that the macroscopic 1D drainage time series of the flow cell can be realistically depicted. However, even after parameter calibration and the manual addition of heterogeneity, the microscopic, heterogeneous 2D distribution of water observed inside the flow cell can only be reproduced qualitatively in our case. This highlights the limitations of Darcy-Richards models, which may be effective at a macroscopic level but fail to represent the internal dynamics of the system accurately. This insight is crucial for the application of Darcy-Richards models and the interpretation of their results, for example, for the calculation of turnover rates of reactive substances depending on the residence times of different water species in specific pore sizes.

Appendix A: Detailed Description of Image Analysis

A first step of the image processing procedure is to prepare the images for the normalization with scattering correction. This includes the removal of outliers and combining a series of open beam and dark images into one single image of each type by applying the pixel-wise median on the series of images. The median dark image is then subtracted from the median open beam image and also from the time series images of the sample to remove the bias introduced by the camera. The same correction is applied to reference images that are needed for the scattering correction. These include images with and without the sample, but instead with a grid of neutron-absorbing dots. The normalization software requires a further dark current image, which is created as a zero-valued image with the exact dimensions as the other images. All these steps are performed using the image processing tool "ImageJ" (Schneider et al., 2012).

The processed images are further corrected for biases introduced by neutron scattering due to sample and instrument background, applying the procedure described by Carminati, Boillat, et al. (2019) and using the image processing tool "KipTool" (Carminati, Strobl, Kaestner, 2019). The normalization also includes correction for fluctuations in source intensity. This procedure provides normalized, gray-level images representing the optical thickness of the object, that is, attenuation coefficient times the thickness. This is proportional to the local water content in the sample.

The finally processed images represent the sum of all attenuating contributions by the sand medium, flow cell, and water. The former two contributions are assumed to be constant throughout the experiment and can be subtracted from all images using the first image of the series. The difference from this subtraction is the attenuation caused only by the water in the sample (Chapter 7 in Strobl & Lehmann, 2024). For further detailed descriptions of the processing of neutron images, we refer to Chapter 20 in Strobl and Lehmann (2024).

However, in our experiments, we observe that additional noise occurs, likely due to jitters and beam fluctuations, which cannot be removed entirely from the background or manually adjusted. Thus, rather than relying on absolute values of water film thicknesses and absolute water masses, we here use relative, normalized water saturation values derived from the rate of change of water content in the image pixels over time, which match the observation (Section 3).

Appendix B: Further Post-Processed Experiment Results

The results in Figure B1 complement those in Figure 8 and further emphasize the heterogeneous nature of the drainage process during the mid-suction phase. It illustrates the relative saturation difference of each grid cell compared to its initial saturation state (WC = 100%) at the start of the mid-suction tension application (249 min). We assume that grid cells losing over 90% of their initial saturation are considered dry, indicated by the color white. The greener a grid cell, the smaller the saturation difference and water loss. In each of the three stable water pockets, between 249 and 350 min, there are individual grid cells with a relative saturation difference of nearly 0. These sand regions remain completely saturated while the surrounding areas have their bulk water removed by the mid-suction tension. This results in a distinctly segregated pattern of water pockets, represented by the entirely white regions between them, especially at 330 and 350 min. There is no significant connection or water film bridge between the pockets.

Figure B2 additionally shows the vertical distribution of relative saturations in the mid-suction phase. For each image in Figure 7, a mean relative saturation value is calculated over each horizontal grid cell row at every vertical position. The vertical grid positions 1–17 correspond to the horizontal grid cell rows located in the air phase, hence maintaining a constant saturation of 0%. Vertical grid positions 18–38 correspond to the horizontal grid cell rows in the continuum. At the beginning (249 min) and end (475 min), saturation is consistently distributed over the vertical extent of images. However, between 290 and 350 min, the saturation distribution exhibits two peaks in

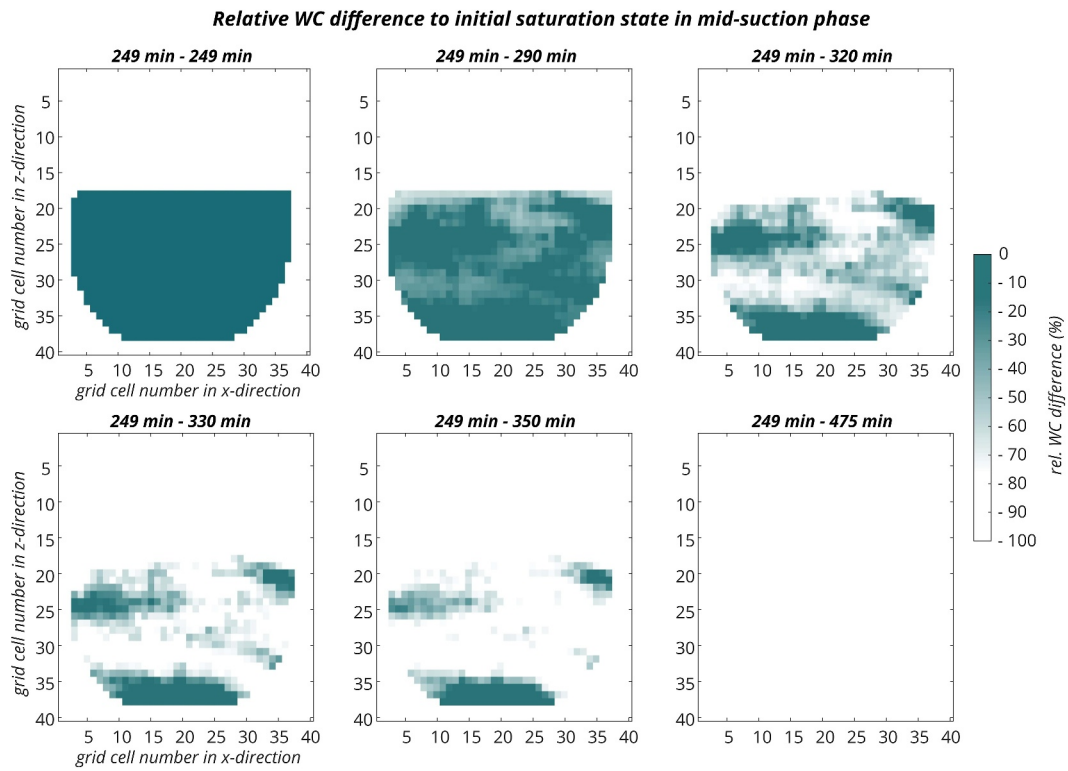

Figure B1. Relative saturation difference of grid cells relative to their initial saturation state at 249 min. The length of 40 grid cells is equal to 1 cm.

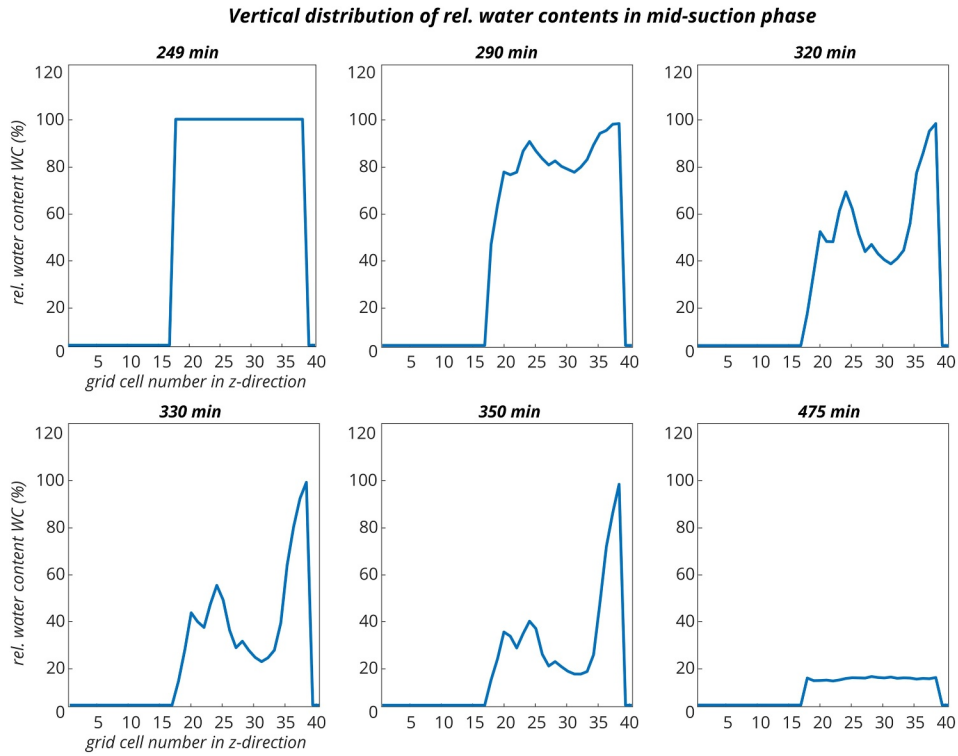

Figure B2. Vertical distribution of relative water contents in the mid-suction phase. Grid cell numbers 1–17 correspond to the horizontal grid cell rows located in the air phase, and numbers 18–38 correspond to the horizontal grid cell rows in the continuum. The length of 40 grid cells is equal to 1 cm.

the vertical positions around 20–25 and 35–38. This bimodal distribution represents the accumulation of water in the three stable water pockets. Water pockets *a* and *b* contribute to the first peak in the vertical positions around 20–25. The mean relative saturation of this peak decreases from approximately 90% to around 40% during this period. Water pocket *c* is reflected in the second peak within the vertical positions around 35–38. Its mean saturation remains relatively constant at approximately 100%, indicating that this is the most persistent water pocket. The finding of a bimodal distribution underpins the heterogeneous, non-continuous conditions for water redistribution in the "homogeneous" flow domain. Homogeneous, continuous conditions are expected to result in a unimodal, left-skewed distribution of saturation over the vertical extent of the flow cell.

Appendix C: Simulations of Internal 2D Water Distribution over Time in Mid-Suction Phase

The following 2D images present the results of the CATFLOW 2D simulations of water distribution inside the flow cell during the drainage process in the mid-suction phase, respectively corresponding to the assumptions (i–iii), proposed in Section 2.2.2. These images represent the temporal evolution of water distribution patterns, and can be compared to the observed patterns shown in Figure 7.

The results based on the initial assumption (i) of a uniform distribution of the derived retention and hydraulic parameters across the continuum, without further calibration, show a completely homogeneous water distribution in the flow cell with no evidence of heterogeneity. The WC is ∼30–40% in all model cells, consistent with the findings from the drainage time series in Figure 9.

The simulation based on assumption (ii) involves a specific adaptation of K_s values in those sand regions where the observations indicate the presence of the three stable water pockets a, b, c (see Figure 7). To achieve the most accurate representation of the observed patterns, we use a K_s value of 3.24×10^{-9} m s^{-1} in pocket *a*, 2.0×10^{-9} m s^{-1} in pocket *b*, and 1.0×10^{-9} m s^{-1} in pocket *c*. All other retention and hydraulic parameters

remain unchanged and correspond to the previous values in Table 2. It is evident from the image after 350 min that this assumption (ii) allows us to replicate the observed patterns of stable water pockets. In general, it can be stated that the observed water patterns in the continuum can indeed be replicated with conventional models, but only when an external forcing is applied through the use of heterogeneously distributed hydraulic properties.

The simulation based on assumption (iii) applies a random noise field for a heterogeneous distribution of K_s values over the continuum. The K_s values are distributed differently in the three stable water pockets, *a*, *b*, and *c*, and in the remaining bulk continuum. In water pocket *a*, the maximum possible K_s value is 3.24×10^{-9} m s^{-1}, in water pocket *b*, it is 2.0×10^{-9} m s^{-1}, and in water pocket *c*, it is 1.0×10^{-9} m s^{-1}, while the K_s value in the bulk continuum remains at the usual value of 3.24×10^{-5} m s^{-1}. In the resulting image, it is visible how the random noise of K_s values leads to more heterogeneous water content patterns within the individual water pockets after 350 min. This result aligns more with the experimental observation, in contrast to the results of the simulation with specifically manipulated and homogeneous K_s values in the respective water pockets (see assumption (ii)). However, no effect of the random K_s noise can be detected outside the water pockets, as the mid-suction tension of 1.14 MPa is too high for the K_s values in the range of 10^{-5} m s^{-1} in the bulk continuum, leading to a smoothing-out of heterogeneities.

C1. 2D Simulation over Time with Assumption (i)

Figure C1 shows 2D water distribution patterns over time in mid-suction phase simulated with assumption (i), based on a uniform distribution of the derived retention and hydraulic parameters across the continuum, without further calibration. After the onset of the mid-suction tension at 249 min, the entire continuum drains gradually and almost entirely by the end of the mid-suction phase at 475 min. This resembles the course of the 1D drainage time series in Figure 9. However, the drainage of the continuum occurs homogeneously throughout its entire extent, without signs of heterogeneous water pockets.

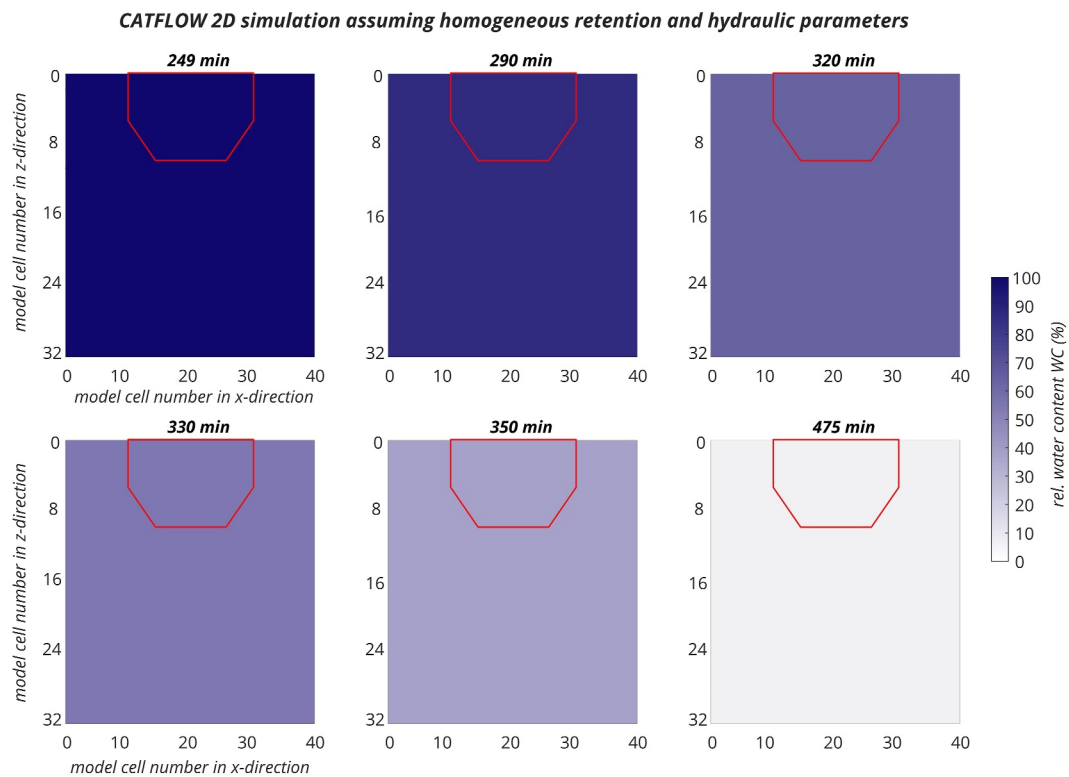

Figure C1. CATFLOW 2D simulation results of internal flow cell processes over time in mid-suction phase, based on assumption (i) (Section 2.2.2) of uniform distribution of retention and hydraulic parameters across the continuum. The length of 20 model cells is equal to 1 cm.

C2. 2D Simulation over Time with Assumption (ii)

Figure C2 presents 2D water distribution patterns over time in mid-suction phase simulated with assumption (ii), which involves a specific adaptation of K_s values in those sand regions where the observations indicate the presence of the three stable water pockets *a*, *b*, *c* (see Figure 7). It is noticeable that the simulated water pockets persist longer than the observed ones, as they remain visible even after 475 min. Moreover, the drainage of the respective water pockets in the simulations proceeds more uniformly over time compared to the observations.

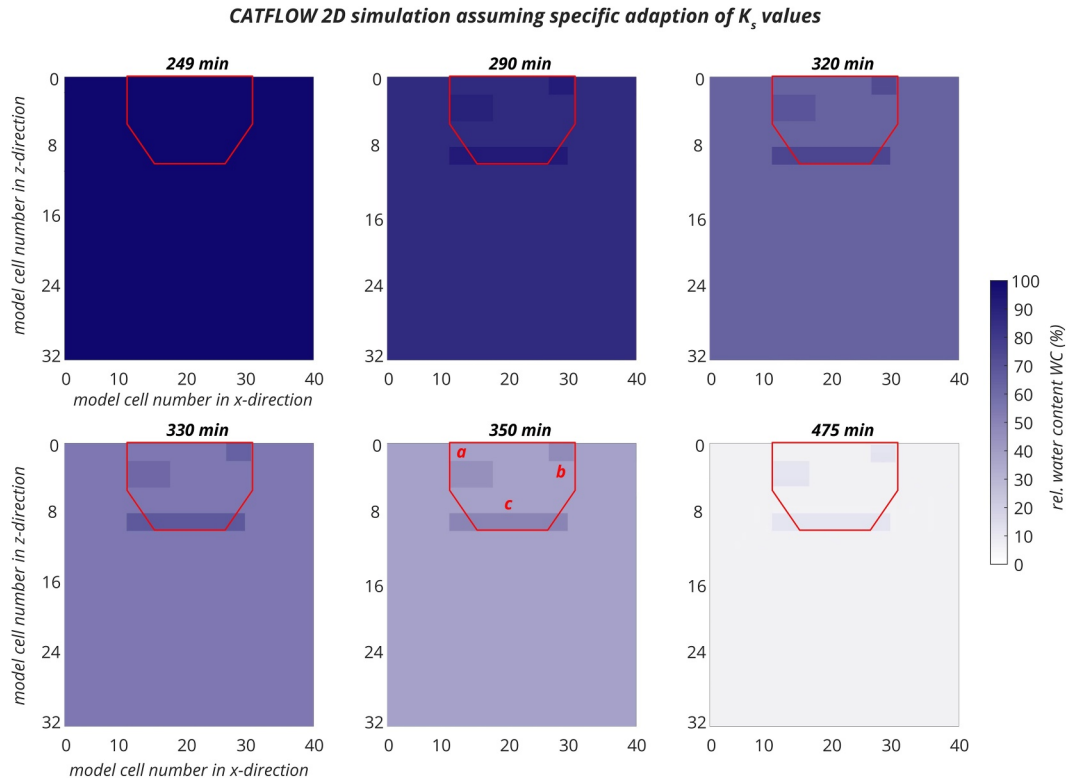

Figure C2. CATFLOW 2D simulation results of internal flow cell processes over time in mid-suction phase, based on assumption (ii) (Section 2.2.2) of specifically adapted K_s values in sand regions according to observed water pockets a, b, c (see Figure 7). The length of 20 model cells is equal to 1 cm.

C3. Simulation with Assumption (iii)

Figure C3 presents 2D water distribution patterns over time in mid-suction phase simulated with assumption (iii), which involves the application of a random noise field for a heterogeneous distribution of K_s values over the continuum. The random noise of K_s values leads to more heterogeneous water content patterns within the individual water pockets throughout the entire mid-suction phase, corroborating the results in Figure 10. However, the water pockets are not visible after 290 min, and they are somewhat too persistent, remaining visible after 475 min.

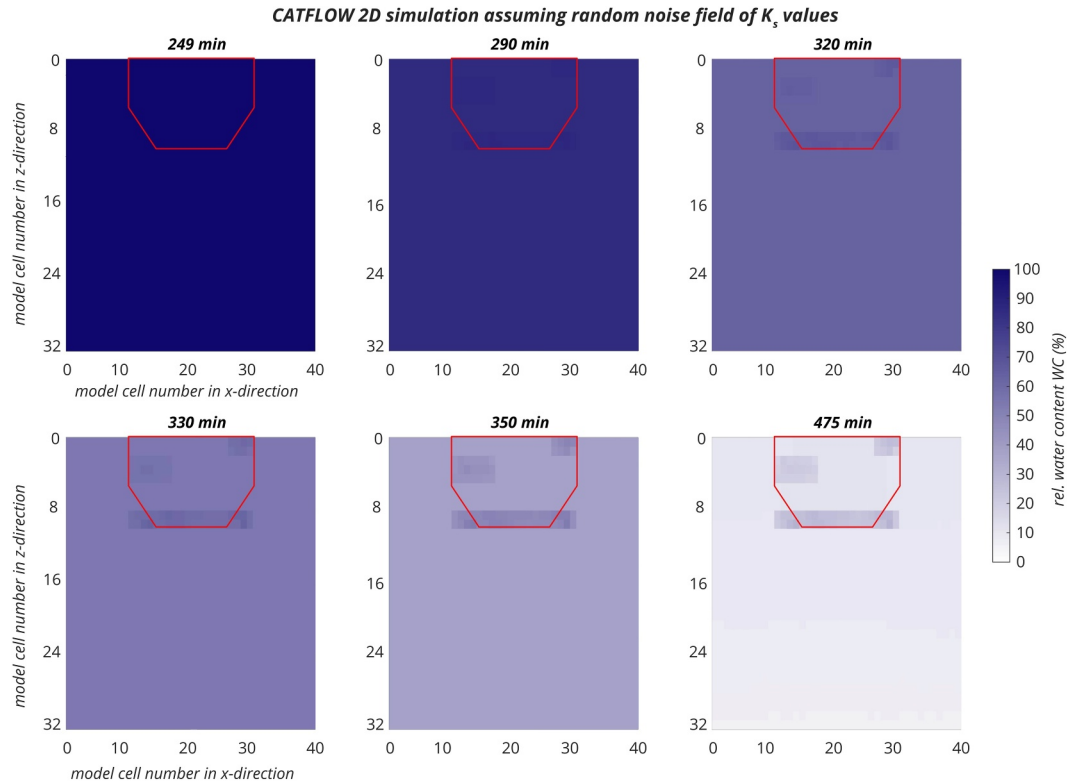

Figure C3. CATFLOW 2D simulation results of internal flow cell processes over time in mid-suction phase, based on assumption (iii) (Section 2.2.2) of applying a random noise field of K_s values over the continuum. 20 model cells equal to 1 cm.

Data Availability Statement

The raw images of the neutron experiment and model data are publicly available and freely accessible on Zenodo: https://doi.org/10.5281/zenodo.11032542 (Sternagel, 2024).

Acknowledgments
The authors declare that they have no conflict of competing financial interest. The authors acknowledge support by Deutsche Forschungsgemeinschaft and the Open Access Publishing Fund of Karlsruhe Institute of Technology (KIT). The service charges for this open access publication have been covered by a Research Centre of the Helmholtz Association. BB gratefully acknowledges the support of a research grant from the Minerva Foundation. RA received funding from the PSI_Cofund project under the European Union's Horizon 2020 research program, as part of the Marie Sklodowska-Curie Grant 701647. This work is based on experiments performed at the Swiss spallation neutron source SINQ, Paul Scherrer Institute, Villigen, Switzerland. We acknowledge Beat Meyer from MicroXAS beamline at the Paul Scherrer Institute for preparing the cell design and also the technical staff at the Karlsruhe Institute of Technology (Institute of Water and Environment) for facilitating the manufacturing process of the experimental flow cell, special acknowledgements go to Michael Ziegler. Open Access funding enabled and organized by Projekt DEAL.

References

Bear, J. (1988). *Dynamics of fluids in porous media*. Dover Publications, Inc.

Berkowitz, B., Dror, I., Hansen, S. K., & Scher, H. (2016). Measurements and models of reactive transport in geological media. *Reviews of Geophysics*, *54*(4), 930–986. https://doi.org/10.1002/2016RG000524

Berkowitz, B., & Hansen, D. P. (2001). A numerical study of the distribution of water in partially saturated porous rock. *Transport in Porous Media*, *45*(2), 301–317. https://doi.org/10.1023/A:1012032723166

Beven, K., & Germann, P. (2013). Macropores and water flow in soils revisited. *Water Resources Research*, *49*(6), 3071–3092. https://doi.org/10.1002/wrcr.20156

Blau, B., Clausen, K. N., Gvasaliya, S., Janoschek, M., Janssen, S., Keller, L., et al. (2009). The Swiss spallation neutron source SINQ at Paul Scherrer Institut. *Neutron News*, *20*(3), 5–8. https://doi.org/10.1080/10448630903120387

Carminati, C., Boillat, P., Schmid, F., Vontobel, P., Hovind, J., Morgano, M., et al. (2019). Implementation and assessment of the black body bias correction in quantitative neutron imaging. *PLoS One*, *14*(1), e0210300. https://doi.org/10.1371/journal.pone.0210300

Carminati, C., Strobl, M., & Kaestner, A. (2019). KipTool, a general purpose processing tool for neutron imaging data. *SoftwareX*, *10*, 100279. https://doi.org/10.1016/j.softx.2019.100279

Carsel, R. F., & Parrish, R. S. (1988). Developing joint probability distributions of soil water retention characteristics. *Water Resources Research*, *24*(5), 755–769. https://doi.org/10.1029/WR024i005p00755

Chen, G., & Flury, M. (2005). Retention of mineral colloids in unsaturated porous media as related to their surface properties. *Colloids and Surfaces A: Physicochemical and Engineering Aspects*, *256*(2), 207–216. https://doi.org/10.1016/j.colsurfa.2005.01.021

Cheng, C.-L., Perfect, E., Donnelly, B., Bilheux, H. Z., Tremsin, A. S., McKay, L. D., et al. (2015). Rapid imbibition of water in fractures within unsaturated sedimentary rock. *Advances in Water Resources*, *77*, 82–89. https://doi.org/10.1016/j.advwatres.2015.01.010

Collins, R., Jenkins, A., & Harrow, M. (2000). The contribution of old and new water to a storm hydrograph determined by tracer addition to a whole catchment. *Hydrological Processes*, *14*(4), 701–711. https://doi.org/10.1002/(SICI)1099-1085(200003)14:4<701::AID-HYP967>3.0.CO;2-2

Cortis, A., & Berkowitz, B. (2004). Anomalous transport in "classical" soil and sand columns. *Soil Science Society of America Journal*, *68*(5), 1539–1548. https://doi.org/10.2136/sssaj2004.1539

Costanza-Robinson, M. S., Estabrook, B. D., & Fouhey, D. F. (2011). Representative elementary volume estimation for porosity, moisture saturation, and air-water interfacial areas in unsaturated porous media: Data quality implications. *Water Resources Research*, *47*(7). https://doi.org/10.1029/2010WR009655

Edery, Y., Guadagnini, A., Scher, H., & Berkowitz, B. (2014). Origins of anomalous transport in heterogeneous media: Structural and dynamic controls. *Water Resources Research*, *50*(2), 1490–1505. https://doi.org/10.1002/2013WR015111

Elrahmani, A., Al-Raoush, R. I., & Seers, T. D. (2023). Clogging and permeability reduction dynamics in porous media: A numerical simulation study. *Powder Technology*, *427*, 118736. https://doi.org/10.1016/j.powtec.2023.118736

Gouet-Kaplan, M., & Berkowitz, B. (2011). Measurements of interactions between resident and infiltrating water in a lattice micromodel. *Vadose Zone Journal*, *10*(2), 624–633. https://doi.org/10.2136/vzj2010.0103

Hager, W. H. (2012). Wilfrid Noel Bond and the Bond number. *Journal of Hydraulic Research*, *50*(1), 3–9. https://doi.org/10.1080/00221686.2011.649839

Hoffman, F., Ronen, D., & Pearl, Z. (1996). Evaluation of flow characteristics of a sand column using magnetic resonance imaging. *Journal of Contaminant Hydrology*, *22*(1), 95–107. https://doi.org/10.1016/0169-7722(95)00079-8

Hoogland, F., Lehmann, P., & Or, D. (2015). The formation of viscous limited saturation zones behind rapid drainage fronts in porous media. *Water Resources Research*, *51*(12), 9862–9890. https://doi.org/10.1002/2015WR016980

Kaestner, A. (2022). Iso-line average tutorial in the "Quantitative Big Imaging" lecture notes. *ETH Zürich*. https://doi.org/10.5281/zenodo.7924608

Kaestner, A., Lehmann, E., & Stampanoni, M. (2008). Imaging and image processing in porous media research. *Advances in Water Resources*, *31*(9), 1174–1187. https://doi.org/10.1016/j.advwatres.2008.01.022

Kirchner, J. W., Feng, X. H., & Neal, C. (2000). Fractal stream chemistry and its implications for contaminant transport in catchments. *Nature*, *403*(6769), 524–527. https://doi.org/10.1038/35000537

Koptyug, I. V. (2012). MRI of mass transport in porous media: Drying and sorption processes. *Progress in Nuclear Magnetic Resonance Spectroscopy*, *65*, 1–65. https://doi.org/10.1016/j.pnmrs.2011.12.001

Kutílek, M., & Nielsen, D. R. (1994). *Soil hydrology: Texbook for students of soil science, agriculture, forestry, geoecology, hydrology, geomorphology and other related disciplines*. Catena Verlag.

Lehmann, E. H., Vontobel, P., & Wiezel, L. (2001). Properties of the radiography facility neutra at SINQ and its potential for use as European reference facility. *Nondestructive Testing and Evaluation*, *16*(2–6), 191–202. https://doi.org/10.1080/10589750108953075

Li, P., & Berkowitz, B. (2018). Controls on interactions between resident and infiltrating waters in porous media. *Advances in Water Resources*, *121*, 304–315. https://doi.org/10.1016/j.advwatres.2018.09.002

Maurer, T. (1997). *Physikalisch begründete, zeitkontinuierliche Modellierung des Wassertransports in kleinen ländlichen Einzugsgebieten*. Mitteilungen des Instituts für Hydrologie und Wasserwirtschaft, Universität Karlsruhe. https://doi.org/10.5445/IR/65797

Menon, M., Robinson, B., Oswald, S. E., Kaestner, A., Abbaspour, K. C., Lehmann, E., & Schulin, R. (2007). Visualization of root growth in heterogeneously contaminated soil using neutron radiography. *European Journal of Soil Science*, *58*(3), 802–810. https://doi.org/10.1111/j.1365-2389.2006.00870.x

Morgano, M., Trtik, P., Meyer, M., Lehmann, E. H., Hovind, J., & Strobl, M. (2018). Unlocking high spatial resolution in neutron imaging through an add-on fibre optics taper. *Optics Express*, *26*(2), 1809–1816. https://doi.org/10.1364/OE.26.001809

Mualem, Y. (1976). A new model for predicting the hydraulic conductivity of unsaturated porous media. *Water Resources Research*, *12*(3), 513–522. https://doi.org/10.1029/WR012i003p00513

Oswald, S., Kinzelbach, W., Greiner, A., & Brix, G. (1997). Observation of flow and transport processes in artificial porous media via magnetic resonance imaging in three dimensions. *Geoderma*, *80*(3), 417–429. https://doi.org/10.1016/S0016-7061(97)00064-5

Rabot, E., Wiesmeier, M., Schlüter, S., & Vogel, H. J. (2018). Soil structure as an indicator of soil functions: A review. *Geoderma*, *314*, 122–137. https://doi.org/10.1016/j.geoderma.2017.11.009

Ranzinger, F., Hille-Reichel, A., Zehe, E., Guthausen, G., & Horn, H. (2020). Quantification of evaporation and drainage processes in unsaturated porous media using magnetic resonance imaging. *Water Resources Research*, *56*(2). https://doi.org/10.23689/fidgeo-4014

Schaap, J. D., Lehmann, P., Kaestner, A., Vontobel, P., Hassanein, R., Frei, G., et al. (2008). Measuring the effect of structural connectivity on the water dynamics in heterogeneous porous media using speedy neutron tomography. *Advances in Water Resources*, *31*(9), 1233–1241. https://doi.org/10.1016/j.advwatres.2008.04.014

Schneider, C. A., Rasband, W. S., & Eliceiri, K. W. (2012). NIH image to ImageJ: 25 years of image analysis. *Nature Methods*, *9*(7), 671–675. https://doi.org/10.1038/nmeth.2089

Shokri, N., Lehmann, P., & Or, D. (2008). Effects of hydrophobic layers on evaporation from porous media. *Geophysical Research Letters*, *35*(19). https://doi.org/10.1029/2008GL035230

Shokri, N., Lehmann, P., Vontobel, P., & Or, D. (2008b). Drying front and water content dynamics during evaporation from sand delineated by neutron radiography. *Water Resources Research*, *44*(6). https://doi.org/10.1029/2007WR006385

Shokri, N., & Sahimi, M. (2012). Structure of drying fronts in three-dimensional porous media. *Physical Review E*, *85*(6), 066312. https://doi.org/10.1103/PhysRevE.85.066312

Sklash, M. G., Stewart, M. K., & Pearce, A. J. (1986). Storm runoff generation in humid headwater catchments: 2. A case study of hillslope and low-order stream response. *Water Resources Research*, *22*(8), 1273–1282. https://doi.org/10.1029/WR022i008p01273

Sprenger, M., Stumpp, C., Weiler, M., Aeschbach, W., Allen, S. T., Benettin, P., et al. (2019). The demographics of water: A review of water ages in the critical zone. *Reviews of Geophysics*, *57*(3), 800–834. https://doi.org/10.1029/2018rg000633

Sternagel, A. (2024). *Data and model files of neutron imaging experiments*. Zenodo. https://doi.org/10.5281/zenodo.11032542

Sternagel, A., Loritz, R., Berkowitz, B., & Zehe, E. (2022). Stepping beyond perfectly mixed conditions in soil hydrological modelling using a Lagrangian approach. *Hydrology and Earth System Sciences*, *26*(6), 1615–1629. https://doi.org/10.5194/hess-26-1615-2022

Sternagel, A., Loritz, R., Klaus, J., Berkowitz, B., & Zehe, E. (2021). Simulation of reactive solute transport in the critical zone: A Lagrangian model for transient flow and preferential transport. *Hydrology and Earth System Sciences*, *25*(3), 1483–1508. https://doi.org/10.5194/hess-25-1483-2021

Sternagel, A., Loritz, R., Wilcke, W., & Zehe, E. (2019). Simulating preferential soil water flow and tracer transport using the Lagrangian Soil Water and Solute Transport Model. *Hydrology and Earth System Sciences*, *23*(10), 4249–4267. https://doi.org/10.5194/hess-23-4249-2019

Strobl, M., & Lehmann, E. (2024). Neutron imaging - From applied materials science to industry. https://doi.org/10.1088/978-0-7503-3495-2

Tang, Y., Yao, X., Chen, Y., Zhou, Y., Zhu, D. Z., Zhang, Y., et al. (2020). Experiment research on physical clogging mechanism in the porous media and its impact on permeability. *Granular Matter*, *22*(2), 37. https://doi.org/10.1007/s10035-020-1001-8

Tumlinson, L. G., Liu, H., Silk, W. K., & Hopmans, J. W. (2008). Thermal neutron computed tomography of soil water and plant roots. *Soil Science Society of America Journal*, *72*(5), 1234–1242. https://doi.org/10.2136/sssaj2007.0302

Turton, D. J., Barnes, D. R., Jr., & de Jesus Návar, J. (1995). Old and new water in subsurface flow from a forest soil block. *Journal of Environmental Quality*, *24*(1), 139–146. https://doi.org/10.2134/jeq1995.00472425002400010020x

van Genuchten, M. T. (1980). A closed-form equation for predicting the hydraulic conductivity of unsaturated soils. *Soil Science Society of America Journal*, *44*, 892–898. https://doi.org/10.2136/sssaj1980.03615995004400050002x

Velásquez-Parra, A., Aquino, T., Willmann, M., Méheust, Y., Le Borgne, T., & Jiménez-Martínez, J. (2022). Sharp transition to strongly anomalous transport in unsaturated porous media. *Geophysical Research Letters*, *49*(3), e2021GL096280. https://doi.org/10.1029/2021GL096280

Zehe, E., & Jackisch, C. (2016). A Lagrangian model for soil water dynamics during rainfall-driven conditions. *Hydrology and Earth System Sciences*, *20*(8), 3511–3526. https://doi.org/10.5194/hess-20-3511-2016

Zehe, E., Maurer, T., Ihringer, J., & Plate, E. (2001). Modeling water flow and mass transport in a loess catchment. *Physics and Chemistry of the Earth - Part B: Hydrology, Oceans and Atmosphere*, *26*(7–8), 487–507. https://doi.org/10.1016/S1464-1909(01)00041-7